

# DRAFT

## CMS Paper

*The content of this note is intended for CMS internal use and distribution only*

2019/06/20

Archive Hash: d9cd38a-D

Archive Date: 2019/06/18

### Measurement of differential $t\bar{t}$ production cross sections for high- $p_T$ top quarks in proton-proton collisions at $\sqrt{s} = 13$ TeV

The CMS Collaboration

#### Abstract

A measurement of the production cross section of high transverse momentum ( $p_T$ ) top quark pairs is reported. The dataset was collected during 2016 with the CMS detector at the CERN LHC from proton-proton collisions at a center-of-mass energy of 13 TeV, and corresponds to an integrated luminosity of  $35.9 \text{ fb}^{-1}$ . The measurement uses events where either both top quark candidates decay hadronically and are reconstructed as large- $R$  jets with  $p_T > 400 \text{ GeV}$ , or where one top quark decays hadronically and is identified as a single large- $R$  jet with  $p_T > 400 \text{ GeV}$  and the other top quark decays leptonically to a  $b$  jet, an electron or a muon, and a neutrino. The cross section is extracted differentially as a function of kinematic variables of the top quark or top quark pair system. The results are unfolded to the particle and parton levels, and are compared to various theoretical models. The measured cross section is significantly lower, by up to 40%, in the phase space of interest, compared to the theory predictions, while the normalized differential cross sections are consistent between data and theory.

This box is only visible in draft mode. Please make sure the values below make sense.

PDFAuthor: Konstantinos Kousouris, Yorgos Tsipolitis, Louise Skinnari, Susan Dittmer  
PDFTitle: Boosted  $t\bar{t}$  in the hadronic and  $l$ -jets channels “(2016 data)”  
PDFSubject: CMS  
PDFKeywords: CMS, physics, top,  $t\bar{t}$ , jets, boosted

Please also verify that the abstract does not use any user defined symbols



# 1 Introduction

The top quark completes the third generation of quarks in the standard model (SM), and the precise knowledge of its properties is critical for the overall understanding of the theory. Measurements of the top-anti-top quark pair ( $t\bar{t}$ ) production cross section confront the predictions from quantum chromodynamics (QCD) and have the potential to constrain the QCD parameters, while being sensitive to physics beyond the SM. Also, the  $t\bar{t}$  production process is a dominant SM background to searches for new physics phenomena and therefore its precise knowledge is essential for new discoveries.

The large  $t\bar{t}$  yield expected in proton-proton (pp) collisions at the CERN LHC allows to perform measurements of the  $t\bar{t}$  production rate in a large phase space, and, more importantly, differentially, as a function of the  $t\bar{t}$  kinematic properties. Such measurements have been performed by the ATLAS [1–6] and CMS [7–15] Collaborations at 7, 8, and 13 TeV center-of-mass energies, under the hypothesis of the resolved final state, where the decay products of the  $t\bar{t}$  pair can be reconstructed individually. This hypothesis is valid for top quark transverse momenta,  $p_T$ , up to approximately 500 GeV. However, at higher  $p_T$ , the top quark decay products are highly collimated (“boosted”) and they can no longer be reconstructed separately. In order to explore the highly boosted phase space, hadronic top quark decays are reconstructed as large-radius jets. Previous efforts in this domain by the ATLAS [16, 17] and CMS [18–20] Collaborations confirm that it is feasible to perform precise differential measurements of the  $t\bar{t}$  production and have also shown interesting deviations from the theory predictions.

In this paper, a measurement of the differential boosted  $t\bar{t}$  production cross section in the hadronic and lepton+jets final states is presented, using pp collisions at  $\sqrt{s} = 13$  TeV recorded with the CMS detector during the 2016 LHC run and amounting to a total integrated luminosity of  $35.9 \text{ fb}^{-1}$ . In the hadronic decay channel, each W boson arising from the top quark decays into a pair of light quarks. As a result, the final state consists of at least six partons (more are possible due to initial- and final-state radiation), two of which are b quarks. Due to the high boost considered in this measurement ( $p_T > 400 \text{ GeV}$ ), the top quarks are reconstructed unambiguously as large-radius jets and the final state consists of at least two such jets. In the lepton+jets channel, one top quark decays to a hadronically-decaying W boson and a b quark ( $t \rightarrow Wb \rightarrow q\bar{q}'b$ ) and is reconstructed as a single large-radius jet, while the second top quark decays to a W boson, which in turn decays to a charged lepton ( $e/\mu$ ) and a neutrino, and a b quark ( $t \rightarrow Wb \rightarrow \ell\nu b$ ).

The paper is organized as follows: Section 2 describes the main features of the CMS detector and the triggering system. Section 3 gives the details of the Monte Carlo simulations. The object reconstruction and the event selection is discussed in Sections 4 and 5, respectively. In Section 6, the estimation of the background contributions is discussed, followed by a discussion of the signal extraction in Section 7. The systematic uncertainties are discussed in Section 8. The unfolding procedure used to obtain the particle- and parton-level cross sections and the results are presented in Section 9. Finally, Section 10 provides the summary of the paper.

## 2 The CMS detector

The central feature of the CMS apparatus is a superconducting solenoid of 6 m internal diameter, providing a magnetic field of 3.8 T. Within the solenoid volume are a silicon pixel and strip tracker, a lead tungstate crystal electromagnetic calorimeter (ECAL), and a brass and scintillator hadron calorimeter (HCAL), each composed of a barrel and two endcap sections. Forward calorimeters extend the pseudorapidity ( $\eta$ ) coverage provided by the barrel and endcap detec-

tors. Muons are detected in gas-ionization chambers embedded in the steel flux-return yoke outside the solenoid. A more detailed description of the CMS detector, together with a definition of the coordinate system used and the relevant kinematic variables, can be found in Ref. [21].

Events of interest are selected using a two-tiered trigger system [22]. The first level (L1), composed of custom hardware processors, uses information from the calorimeters and muon detectors to select events at a rate of around 100 kHz within a time interval of less than  $4\ \mu\text{s}$ . The second level, known as the high-level trigger (HLT), consists of a farm of processors running a version of the full event reconstruction software optimized for fast processing, and reduces the event rate to around 1 kHz before data storage.

### 3 Monte Carlo event generation

Monte Carlo simulation is used to generate samples for the  $t\bar{t}$  signal and to model the kinematic distributions of some of the background processes. Samples of simulated  $t\bar{t}$  events have been generated at next-to-leading order (NLO) in QCD using POWHEG v2 [23–27], assuming a top quark mass of  $m_t = 172.5\ \text{GeV}$ . Single top quark production in the  $t$  channel or in association with a W boson are simulated at NLO with POWHEG [28]. The production of W or Z bosons in association with jets (V+jets), as well as QCD multijet events, are simulated with MG5\_AMC@NLO [29] at leading order (LO), with the MLM matching algorithm [30]. Samples of diboson (WW, WZ, ZZ) events are simulated using PYTHIA 8.

All simulated events are processed with PYTHIA 8.212 [31, 32] for modeling of the parton showering, hadronization, and underlying event (UE). The NNPDF 3.0 [33] Parton Distribution Functions (PDF) are used throughout, and the CUETP8M1 UE tune [34] is used for all processes except for the  $t\bar{t}$ ,  $t\bar{t}H$  and single top quark processes, for which the tune CUETP8M2T4 [35] is used. The Simulation of the CMS detector response is based on GEANT4 [36]. Additional pp interactions in the same or neighbouring bunch crossings (pileup) are simulated with PYTHIA and overlaid with generated events according to the pileup distribution measured in data.

The various simulated processes are normalized to the best known theoretical cross sections, namely the  $t\bar{t}$ , V+jets, and single top quark samples are normalized to NNLO precision in QCD [37–39].

The measured cross sections for the  $t\bar{t}$  process are compared to theoretical predictions provided by the following Monte Carlo models: POWHEG combined with PYTHIA for the parton showering, as described above, or combined with HERWIG ++ [40] and the corresponding EE5C UE tune [41]. In addition,  $t\bar{t}$  events were also generated with MC@NLO [29] combined with PYTHIA for the parton showering.

### 4 Object reconstruction

The global event reconstruction (also called particle-flow event reconstruction [42]) aims to reconstruct and identify each individual particle in an event, with an optimized combination of all subdetector information. In this process, the identification of the particle type (photon, electron, muon, charged hadron, neutral hadron) plays an important role in the determination of the particle direction and energy. Photons (e.g. coming from  $\pi^0$  decays or from electron bremsstrahlung) are identified as ECAL energy clusters not linked to the extrapolation of any charged particle trajectory to the ECAL. Electrons (e.g. coming from photon conversions in the tracker material or from B hadron semileptonic decays) are identified as a primary charged

particle track and potentially many ECAL energy clusters corresponding to this track extrapolation to the ECAL and to possible bremsstrahlung photons emitted along the way through the tracker material. Muons (e.g. from B hadron semileptonic decays) are identified as tracks in the central tracker consistent with either a track or several hits in the muon system, and associated with calorimeter deposits compatible with the muon hypothesis. Charged hadrons are identified as charged particle tracks neither identified as electrons, nor as muons. Finally, neutral hadrons are identified as HCAL energy clusters not linked to any charged hadron trajectory, or as a combined ECAL and HCAL energy excess with respect to the expected charged hadron energy deposit.

The energy of photons is obtained from the ECAL measurement. The energy of electrons is determined from a combination of the track momentum at the main interaction vertex, the corresponding ECAL cluster energy, and the energy sum of all bremsstrahlung photons attached to the track. The energy of muons is obtained from the corresponding track momentum. The energy of charged hadrons is determined from a combination of the track momentum and the corresponding ECAL and HCAL energies, corrected for zero-suppression effects and for the response function of the calorimeters to hadronic showers. Finally, the energy of neutral hadrons is obtained from the corresponding corrected ECAL and HCAL energies.

Leptons and charged hadrons are required to be compatible with originating from the primary interaction vertex. The reconstructed vertex with the largest value of summed physics-object  $p_T^2$  is taken to be the primary pp interaction vertex. The physics objects are the jets, clustered using the jet finding algorithm with the tracks assigned to the vertex as inputs, and the associated missing transverse momentum, taken as the negative vector sum of the  $p_T$  of those jets. Charged hadrons that are associated with a pileup vertex are classified as pileup candidates and are ignored in the subsequent object reconstruction. Electron and muon objects are first identified from corresponding electron or muon particle-flow candidates. Next, jet clustering is performed on all particle-flow candidates that are not classified as pileup candidates. The jet clustering does not exclude the electron and muon particle-flow candidates, even if these have already been assigned to electron/muon objects. A dedicated overlap removal is therefore applied at analysis level to avoid double-counting.

Muons and electrons are required to have  $p_T > 50(30)$  GeV and  $|\eta| < 2.1$  for the l+jets (hadronic) channel. Leptons must also be isolated according to the “mini isolation” ( $I_{mini}$ ) algorithm, which requires the  $p_T$  sum of tracks in a cone around the muon or electron to be less than a given fraction of the lepton  $p_T$ . The cone width varies with the lepton  $p_T$  as  $R = 10/p_T^\ell$  for  $p_T^\ell < 200$  GeV and  $R = 0.05$  for  $p_T^\ell > 200$  GeV. A cut value of  $I_{mini} < 0.1$  is used. A looser selection is used to define veto leptons for the l+jets channel, requiring  $p_T > 50$  GeV and  $|\eta| < 2.1$ , but no isolation requirement. Correction factors are applied to account for differences between data and the simulation in the modeling of the lepton identification and trigger efficiencies, determined as a function of the muon/electron  $|\eta|$  and  $p_T$ .

For each event, hadronic jets are clustered from the particles reconstructed by the particle-flow algorithm using the infrared and collinear safe anti- $k_T$  algorithm [43, 44]. Two different jet collections are considered for the analysis. Small- $R$  jets are clustered using a distance parameter of 0.4 (used for the l+jets channel) and large- $R$  jets using a distance parameter of 0.8 (used for the l+jets and hadronic channels). The jet momentum is determined as the vectorial sum of all particle momenta in the jet, and is found from simulation to be, on average, within 5 to 10% of the true momentum over the whole  $p_T$  spectrum and detector acceptance. Additional proton-proton interactions within the same or nearby bunch crossings (pileup) can contribute additional tracks and calorimetric energy depositions to the jet momentum. To mitigate this

effect, charged particles identified to be originating from pileup vertices are discarded and an offset correction is applied to correct for remaining contributions.

Jet energy corrections are derived from simulation to bring the measured response of jets to that of particle-level jets on an average. In situ measurements of the momentum balance in dijet, photon + jet, Z + jet, and multijet events are used to account for any residual differences in jet energy scale between data and simulation [45]. The jet energy resolution amounts typically to 15% at 10 GeV, 8% at 100 GeV, and 4% at 1 TeV. Additional selection criteria are applied to each jet to remove jets potentially dominated by anomalous contributions from various subdetector components or reconstruction failures.

In order to identify jets originating from hadronic decays of top quarks (t tagged) we use the 3-subjettiness, 2-subjettiness, and 1-subjettiness variables [46],  $\tau_3$ ,  $\tau_2$ , and  $\tau_1$  computed using the jet constituents, according to the Eq. 1. In this algorithm, the constituents of the large- $R$  jets are reclustered using the Cambridge–Aachen algorithm [47, 48].

$$\tau_N = \frac{1}{\sum_k p_{T,k} R} \sum_k p_{T,k} \min\{\Delta R_{1,k}, \Delta R_{2,k}, \dots, \Delta R_{N,k}\}, \quad (1)$$

where  $N$  denotes the reconstructed candidate subjects and  $k$  runs over the constituent particles in the jet. The variable  $\Delta R_{i,k} = \sqrt{(\Delta y_{i,k})^2 + (\Delta \phi_{i,k})^2}$  is the angular distance between the candidate subject  $i$  and the particle  $k$ . The variable  $R$  is the characteristic jet radius ( $R = 0.8$  in our case).

In addition, a grooming technique is applied to remove soft, wide-angle radiation from the jet and to improve the mass resolution. The algorithm employed is the “modified mass drop tagger” [49, 50], also known as the *soft drop* (SD) algorithm [51], with angular exponent  $\beta = 0$ , soft cutoff threshold  $z_{\text{cut}} < 0.1$ , and characteristic radius  $R_0 = 0.8$  [51].

Small- $R$  jets and subjects of the large- $R$  jets are identified as b quark candidates (b tagged) using the Combined Secondary Vertex (CSV) algorithm [52]. Data-to-simulation correction factors are used to match the b tagging efficiency observed in simulation to that measured in data.

The missing transverse momentum vector  $\vec{p}_T^{\text{miss}}$  is defined as the projection on the plane perpendicular to the beams of the negative vector sum of the momenta of all particle flow candidates in an event. Its magnitude is referred to as  $p_T^{\text{miss}}$ .

## 5 Event selection

### 5.1 Trigger

Different triggers were employed for the collection of signal events in the l+jets and hadronic channels according to each event topology. The trigger employed in the hadronic channel required the presence of a jet with  $p_T > 180$  GeV at L1. At HLT, large- $R$  jets were reconstructed from particle-flow candidates using the anti- $k_T$  algorithm with a distance parameter of 0.8. The mass of the jets at HLT, after removal of soft particles, was required to be greater than 30 GeV. The selected events contained at least two such jets with  $p_T > 280(200)$  GeV for the leading (trailing) one. Finally, at least one of these jets was b tagged, using the CSV algorithm suitably adjusted for HLT, with an average efficiency of 90% for b jets. The aforementioned trigger ran for the entire 2016 run, collecting an integrated luminosity of  $35.9 \text{ fb}^{-1}$ . A second trigger with identical kinematic requirements but no b tagging, was employed and ran on average every



21 bunch crossings, collecting an integrated luminosity of  $1.67 \text{ fb}^{-1}$ . The events collected with the latter trigger are used for the selection of a control sample for estimating the QCD multijet background, as described later. For the l+jets channel, the data were selected using triggers requiring a single lepton, either a muon with  $p_T > 40 \text{ GeV}$  and  $|\eta| < 2.1$  or an electron with  $p_T > 45 \text{ GeV}$ , with no isolation criteria applied, as well as two jets with  $p_T > 200, 50 \text{ GeV}$ .

## 5.2 Hadronic channel

The baseline selection is common for all regions used in the hadronic analysis and it requires at least two large- $R$  jets in the event with  $p_T > 400 \text{ GeV}$  and soft-drop masses in the range  $50\text{--}300 \text{ GeV}$ . Also, events with at least one lepton (muon or electron) are vetoed in order to suppress leptonic top decays.

In order to discriminate between events that originate from  $t\bar{t}$  decays vs QCD multijet production, the jet substructure variables are utilized. These variables are sensitive to the type of the jet, and in particular to whether it comes from a single-prong decay, like ordinary quark or gluon jets, or from a three-prong decay, such as the  $t \rightarrow Wb \rightarrow \bar{q}q'b$  decay that is of interest here. The  $\tau_{1,2,3}$  variables of the two leading, large- $R$  jets are combined with a neural network (NN) to form a multivariate event discriminant. The NN consists of two hidden layers with 16 and 4 nodes, respectively, and is implemented with the TMVA toolkit [53]. The NN output characterizes each event, with values close to zero indicating QCD dijet production and values close to one suggesting  $t\bar{t}$  production.

On top of the baseline selection, various regions are defined based on the NN output, the jets soft-drop masses, and the number of  $b$  tagged subjets in each large- $R$  jet, that serve different analysis purposes. The signal region ( $SR$ ) is where the differential measurements are performed and it requires both jets to have a  $b$  tagged subjet, a tighter selection on the jets' masses ( $120\text{--}220 \text{ GeV}$ ), and an NN output value greater than 0.8. In this selection, more than 95% of the events come from hadronic top decays. The QCD control region ( $CR$ ) is the same as the  $SR$  but with the  $b$  tagging requirement inverted (the jets should not contain a  $b$  tagged subjet) and it is used to get from data the shape of the QCD background for each variable of interest. The signal region A ( $SR_A$ ) requires the baseline selection plus  $NN > 0.8$  and both jets to have a  $b$  tagged subjet, while the corresponding control region ( $CR_A$ ) has the  $b$  tagging condition reverted. These regions are used to determine the normalization of the QCD background. Finally, the signal region B ( $SR_B$ ) is used to constrain some of the signal modeling uncertainties and is the same as  $SR$  but without any NN requirement. Figure 1 shows the distribution of the NN output in  $SR_B$  and Fig. 2 shows the N-subjettiness variables for the two leading large- $R$  jets. Figure 4 shows the soft-drop mass of the  $b$  tagged and non  $b$  tagged subjets of the two leading large- $R$  jets.

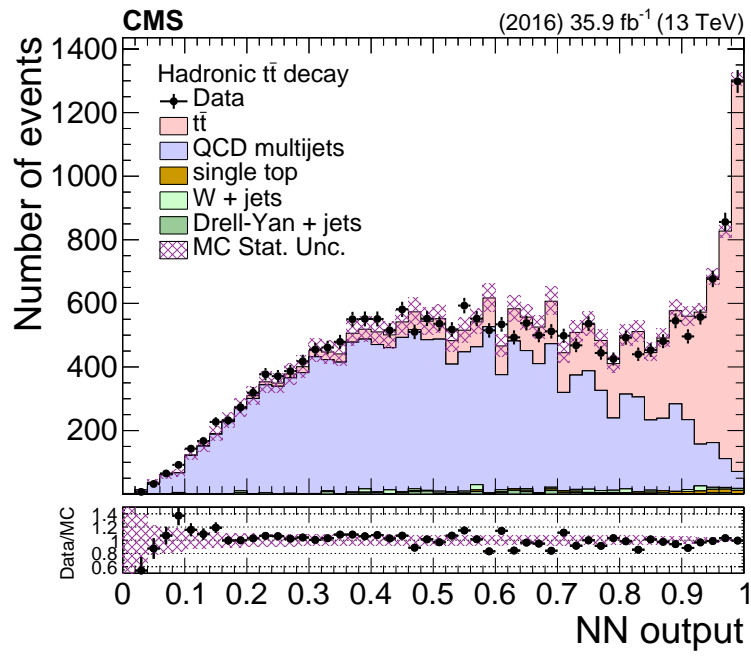


Figure 1: Data vs simulation in  $SR_B$  for the NN output in the hadronic channel.



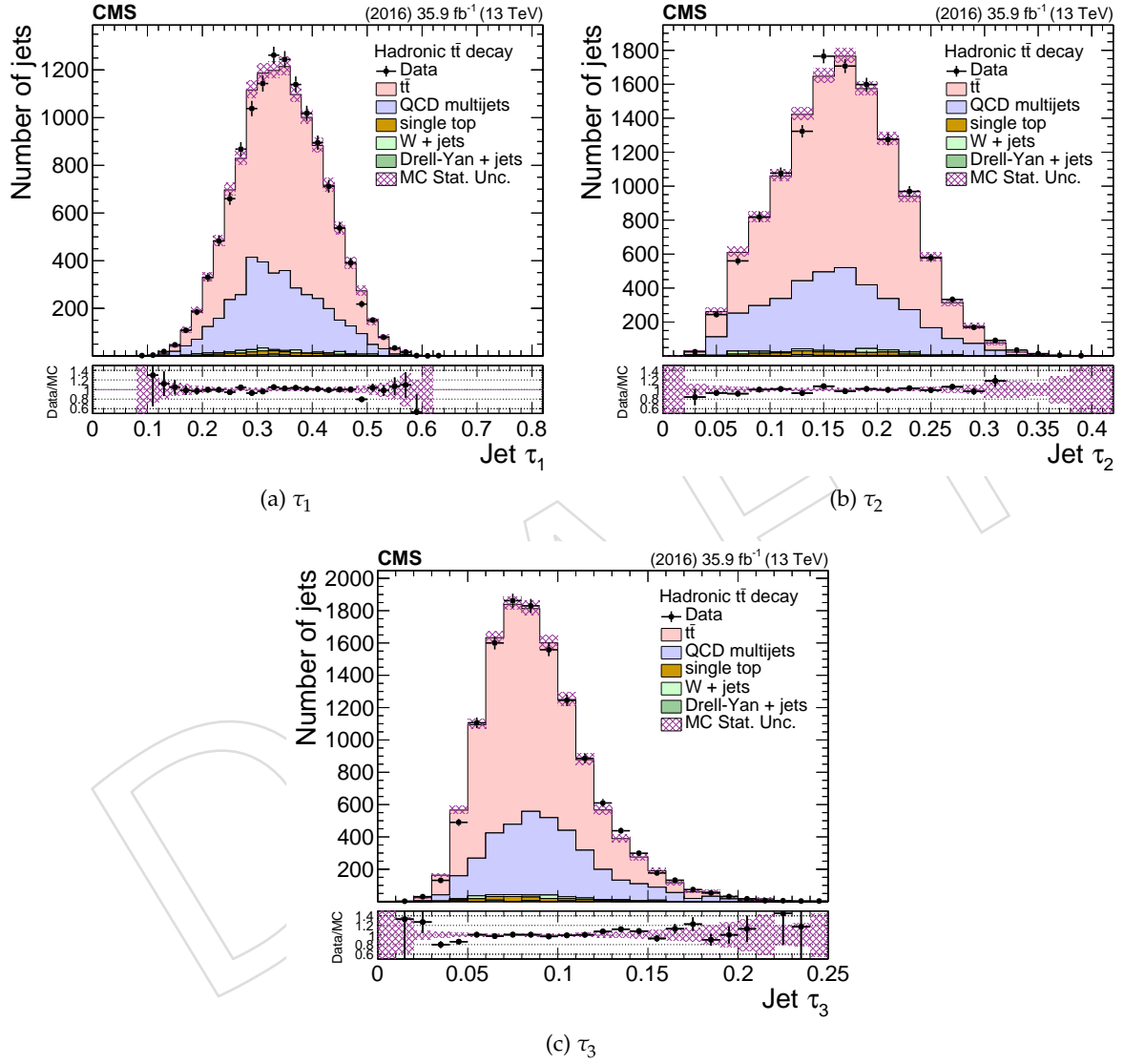


Figure 2: Data vs simulation in the signal region for the N-subjettiness variables of the two leading large- $R$  jets in the hadronic channel.

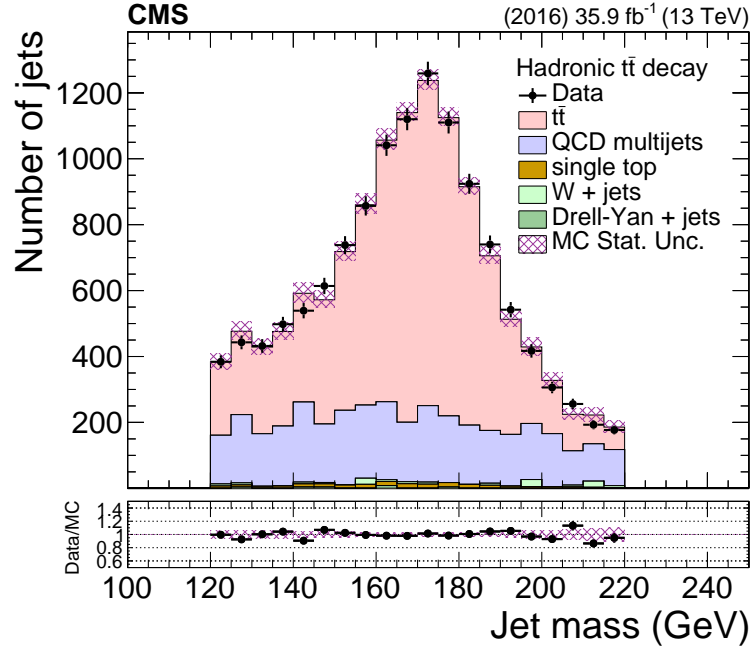


Figure 3: Data vs simulation in the signal region for the mass of the two leading large- $R$  jets in the hadronic channel.

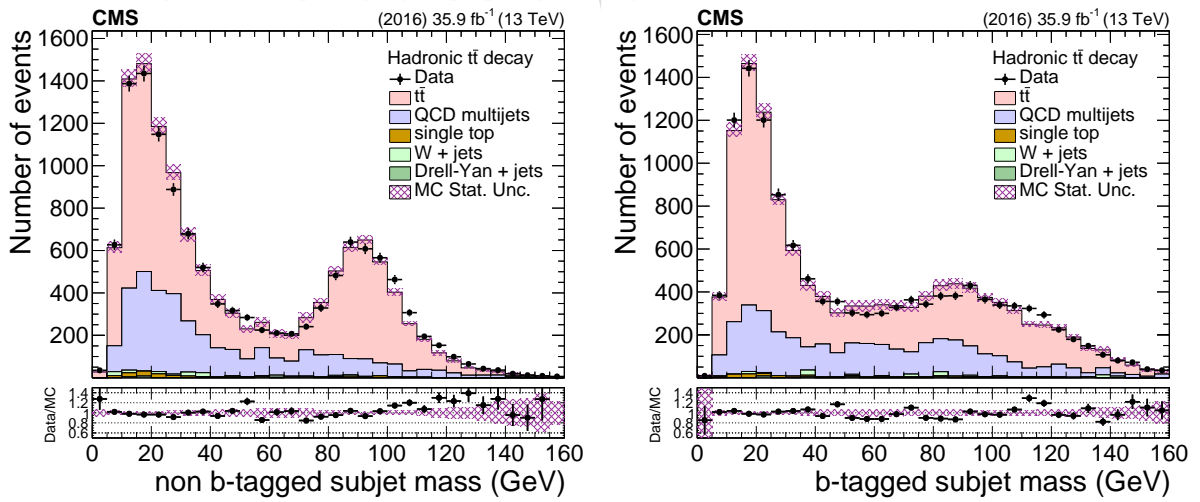


Figure 4: Data vs simulation in the signal region for the mass of the  $b$  tagged (left) and non  $b$  tagged (right) subject of the two leading large- $R$  jets in the hadronic channel.

### 5.3 Lepton+jets channel

The lepton+jets final state is identified through the presence of an electron or a muon, a small- $R$  jet assumed to be produced by the decay of the  $b$  quark from the leptonic top quark decay, and a large- $R$  jet corresponding to the hadronically decaying top quark.

Small- $R$  jets, i.e. anti- $k_t$  jets with a size parameter of 0.4, are required to have  $p_T > 50 \text{ GeV}$  and  $|\eta| < 2.4$ . Large- $R$  jets (anti- $k_t$  jets with a size parameter of 0.8) must fulfill  $p_T > 400 \text{ GeV}$  and  $|\eta| < 2.4$ . Since the particle-flow candidates ultimately identified as muons or electrons are initially used in the jet clustering, these leptons are removed from the collection of jets at analysis level to avoid double-counting. No reclustering is performed after the jet cleaning.

Events are required to first pass a so-called preselection, defined as follows:

- Exactly one signal muon or signal electron.
- Zero additional veto leptons.
- At least one leptonic-side jet (small- $R$  jet in the same hemisphere as the signal lepton,  $0.3 < \Delta R(\ell, \text{jet}) < \pi/2$ ).
- At least one hadronic-side jet (large- $R$  jet in the opposite hemisphere from the signal lepton,  $\Delta R(\ell, \text{jet}) > \pi/2$ ).
- $p_T^{\text{miss}} > 35 \text{ GeV}$  (muon channel) or  $> 50 \text{ GeV}$  (electron channel).
- For events in the electron channel: ‘triangular’ cut,  $|\Delta\phi(X, p_T^{\text{miss}})| < 1.5 \cdot \frac{p_T^{\text{miss}}}{7 \text{ GeV}}$  for both  $X = \text{electron}$  and  $X = \text{leading small-}R \text{ jet}$ .

The more stringent  $p_T^{\text{miss}}$  criteria and the triangular cut in the electron channel are applied to further reduce background from QCD multijet production.

Events that fulfill the preselection criteria are further categorized based on whether the  $b(t)$  jet candidate passes or fails the  $b(t)$  tagging criteria. The  $N$ -subjettiness ratio  $\tau_3/\tau_2$  (abbreviated as  $\tau_{32}$ ) is used as the sensitive variable to distinguish a three-prong hadronic top quark decay from background processes, requiring  $\tau_{32} < 0.81$ . A data-to-simulation efficiency correction factor is extracted simultaneously with the integrated signal yield, as described in Section 7, to correct the  $t$  tagging efficiency in simulation to match that in data. The  $b(t)$  jet candidate is the highest- $p_T$  leptonic-side (hadronic-side) jet in the event. Events are divided into the following categories:

- 0  $t$  tag (0t):  $t$  jet candidate fails the  $t$  tagging requirement.
- 1  $t$  tag 0  $b$  tag (1t0b):  $t$  jet candidate passes the  $t$  tagging requirement, but  $b$  jet candidate fails the  $b$  tagging requirement.
- 1  $t$  tag 1  $b$  tag (1t1b): both  $t$  jet candidate and  $b$  jet candidate pass their respective tagging requirement.

These event categories are designed to have different admixtures of signal and background, with the 0t region being the most background dominated and the 1t1b region the most signal dominated.

## 6 Background estimation

The dominant background in the hadronic channel is the QCD multijet production, while the dominant background processes contributing in the  $l$ +jets channel include non-signal  $t\bar{t}$ , single top quark,  $W$ +jets, and QCD multijet production. Non-signal  $t\bar{t}$  comprises dileptonic and

hadronic final states, in addition to  $\tau$ +jets events where the tau lepton does not decay to a muon or an electron.

In the hadronic channel, the QCD background is suppressed significantly with a combination of b tagging requirements on the subjets and N-subjettiness variables. The remaining contribution is estimated from a control data sample. The two elements that are determined from data are the shape  $Q(x)$  of the QCD background as a function of an observable of interest  $x$ , and the absolute normalization  $N_Q$ . The QCD template  $Q(x)$  is taken from the QCD control sample by applying the signal region selection with inverted b tagging requirement (none of the leading large- $R$  jets is allowed to contain a b tagged subjet). The  $t\bar{t}$  contamination of the control sample, based on the simulation, is of the order of 1%. The normalization of the QCD background is determined from a fit to the data in  $SR_A$  on the soft-drop mass of the top jet candidate (this is taken as the leading large- $R$  jet). However, since this is an extended signal region (in order to allow for QCD dominated sidebands), a transfer factor  $R_{\text{yield}}$  is needed in order to get the QCD normalization in the signal region. The value of  $R_{\text{yield}}$  is independent of the b tagging requirement and therefore it is taken from the QCD control data sample. The subdominant background processes, namely single top quark production and vector bosons produced in association with jets, have a negligible contribution in the signal region (below 1% in the entire phase space) and are estimated from the simulation.

In the l+jets channel, background events due to non-signal  $t\bar{t}$ , single top quark, W/Z+jets, and diboson production are estimated from simulation. The QCD multijet background is modeled with data-driven techniques, using a data sideband region dominated by multijet events. The sideband is defined by inverting the isolation requirement on the lepton and relaxing the lepton identification criteria. The predicted contributions to the sideband region from signal and other background events are subtracted from the observed data in the sideband to yield the kinematic distributions for QCD multijet events. The normalization of the multijet background is extracted from a maximum-likelihood fit, described in Section 7.2, but an initial estimate of its normalization is taken from the simulated prediction in the signal region. Also the normalization of the other background processes is constrained through the fit.

## 7 Signal extraction

### 7.1 Hadronic channel

The  $t\bar{t}$  signal is extracted from data, differentially, as a function of five variables: (inclusive) top  $p_T$  and  $\eta$ ,  $t\bar{t}$  mass,  $p_T$ , and rapidity, by subtracting the contribution of the backgrounds:

$$S(x) = D(x) - R_{\text{yield}} N_{\text{qcd}} Q(x) - B(x), \quad (2)$$

where  $x = p_T^t, \eta^t, m^{t\bar{t}}, p_T^{t\bar{t}}, y^{t\bar{t}}$ ,  $S(x)$  is the  $t\bar{t}$  signal,  $D(x)$  is the measured distribution in data,  $Q(x)$  is the QCD shape,  $B(x)$  is the subdominant backgrounds' contribution (both the shape and the normalization are taken from the simulation),  $R_{\text{yield}} = N^{CR}/N^{CR_A}$  is equal to the yield ratio between  $SR$  and  $SR_A$ , and  $N_{\text{qcd}}$  is the fitted number of QCD events in  $SR_A$ .

The quantity  $N_{\text{qcd}}$  is estimated from a maximum likelihood fit to the data in  $SR_A$  on the mass of the top candidate, which is the soft-drop mass of the leading large- $R$  jet. The fit is described by the equation below:

$$D(m^t) = N_{t\bar{t}} T(m^t; k_{\text{scale}}, k_{\text{res}}) + N_{\text{qcd}} (1 + k_{\text{slope}} m^t) Q(m^t) + N_{\text{bkg}} B(m^t) \quad (3)$$

which contains the shapes  $T(m^t)$ ,  $B(m^t)$  of the signal and the subdominant backgrounds, respectively, taken from the simulation, and the shape  $Q(m^t)$  of the QCD multijet background, taken from the control sample in data. To account for a possible QCD shape difference on the  $m^t$  variable between the control and signal regions, a linear modification factor  $(1 + k_{\text{slope}} m^t)$  is introduced, inspired by the simulation, but with the slope parameter  $k_{\text{slope}}$  left free in the fit. Also free in the fit are the normalization factors  $N_{t\bar{t}}$ ,  $N_{\text{qcd}}$ , and  $N_{\text{bkg}}$ . Finally, two more nuisance parameters are introduced in the simulated  $t\bar{t}$  shape,  $k_{\text{scale}}$  and  $k_{\text{res}}$ , which account for possible differences between data and simulation in the scale and resolution of the  $m^t$  parameter. The fit model is performed with the ROOFIT toolkit [54] and the fit result is shown in Figure 5. The fitted  $t\bar{t}$  yield (6238) is significantly lower than the expectation (9604), which implies that the fiducial cross section is  $\approx 35\%$  lower compared to the POWHEG +PYTHIA prediction.

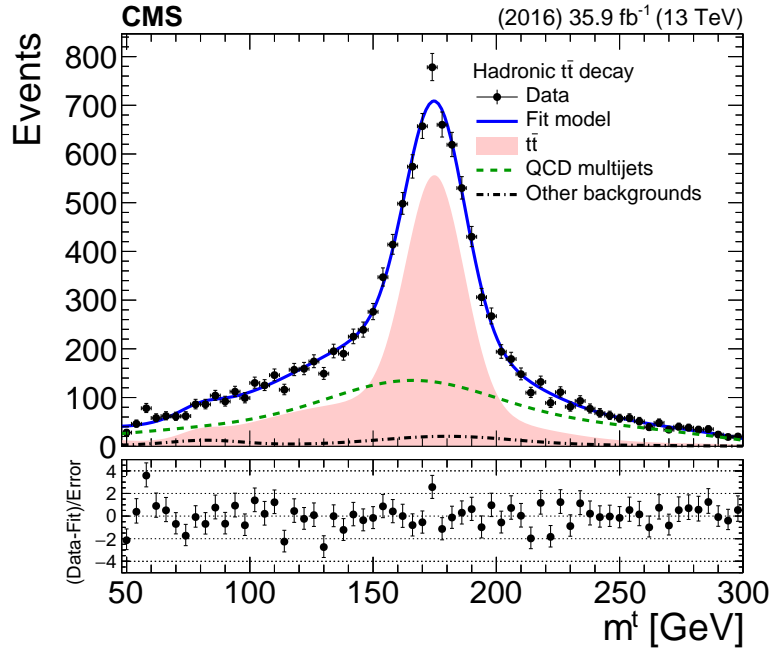


Figure 5: Result of the fit on data in  $SR_A$  in the hadronic channel. The shaded area shows the  $t\bar{t}$  contribution, the dashed line shows the QCD multijet background, and the double-dashed line shows the other subdominant backgrounds. The solid line shows the combined signal plus background fit model.

## 7.2 Lepton+jets channel

For the l+jets analysis, the signal strength,  $t$  tagging efficiency scale factor, and background normalizations are determined in a simultaneous binned maximum-likelihood fit to the data across the different analysis event categories.

The  $0t$ ,  $1t0b$ , and  $1t1b$  event categories are fitted simultaneously, normalizing each background component to the same cross section in all categories. The fit result is expressed in terms of a multiplicative factor, the signal strength  $r$ , applied to the input  $t\bar{t}$  cross section. Different variables are used to discriminate the  $t\bar{t}$  signal from the background processes. The small- $R$  jet  $\eta$  distribution is used in the  $0t$  and  $1t0b$  categories, while the large- $R$  jet soft-drop mass distribution is used in the  $1t1b$  region. These distributions were chosen to have good discrimination between  $t\bar{t}$ ,  $W$ +jets, and QCD multijet production. The  $t\bar{t}$  signal and  $t\bar{t}$  background distributions are merged into a single distribution for the purpose of the fit, essentially constraining the semileptonic branching ratio to be equal to that provided by the simulation.

Background normalizations and experimental sources of systematic uncertainty are treated as nuisance parameters in the fit. The uncertainties due to pileup reweighting, lepton scale factors, jet energy scale and resolution, b tagging efficiency, and t tagging efficiency are treated as uncertainties in the distribution of the input templates. Two nuisance parameters are used to describe the t tagging uncertainty: a t tag scale factor nuisance parameter is applied to the  $t\bar{t}$  and single top quark samples, where we expect the t tagged jet to correspond to a true top quark decay, while a t mis-tag scale factor is applied for the W+jets and QCD multijet samples. The uncertainties in the luminosity and background normalizations are treated as rate uncertainties. The event categories that are fitted are designed such that the t tagging efficiency is constrained by the relative population of events in the three categories. The varying admixtures of signal and background between the different regions provide power to determine the background normalizations. The measurement of the  $t\bar{t}$  cross section is correlated with the various nuisance parameters, with the strongest correlation being with the t tagging efficiency, as expected. For the shape uncertainties, the nuisance parameter is used to interpolate between the nominal kinematic distribution and distributions corresponding to  $\pm 1\sigma$  variations in the given uncertainty. The uncertainties due to the theoretical modeling are evaluated independently from the fit.

The  $e/\mu$ +jets channels are fitted together, with all nuisance parameters generally constrained to be the same in both channels. The nuisance parameters associated with the electron and muon scale factors are treated separately, as are the muon and electron QCD multijet background normalizations. The posterior kinematic distributions for the three fit categories are shown in Figure 6. The event counts that account for all posterior parameters are given in Table 1.

Sample	Number of events ( $\mu$ +jets channel)		
	0t	1t0b	1t1b
$t\bar{t}$	$18300 \pm 1744$	$4226 \pm 189$	$3865 \pm 94$
Single t	$3209 \pm 719$	$263 \pm 81$	$144 \pm 39$
W+jets	$22070 \pm 2919$	$2456 \pm 336$	$104 \pm 21$
Z+jets	$2249 \pm 597$	$216 \pm 68$	$18 \pm 10$
Diboson	$550 \pm 176$	$34 \pm 12$	$2 \pm 1$
Multijet	$2761 \pm 1219$	$166 \pm 79$	$46 \pm 25$
Total	$49140 \pm 3735$	$7360 \pm 408$	$4179 \pm 107$
Data	49137	7348	4187

Sample	Number of events (e+jets channel)		
	0t	1t0b	1t1b
$t\bar{t}$	$9668 \pm 1314$	$2907 \pm 126$	$2729 \pm 68$
Single t	$1978 \pm 400$	$178 \pm 52$	$98 \pm 27$
W+jets	$15300 \pm 2320$	$1384 \pm 205$	$56 \pm 12$
Z+jets	$1351 \pm 378$	$134 \pm 46$	$19 \pm 17$
Diboson	$378 \pm 104$	$20 \pm 7$	$2 \pm 1$
Multijet	$2879 \pm 1328$	$208 \pm 111$	$22 \pm 23$
Total	$31555 \pm 3030$	$4831 \pm 274$	$2925 \pm 80$
Data	31559	4801	2953

Table 1: Posterior signal and background normalizations in the 0t, 1t0b, and 1t1b regions, together with observation in data. The uncertainties include all post-fit experimental uncertainties.

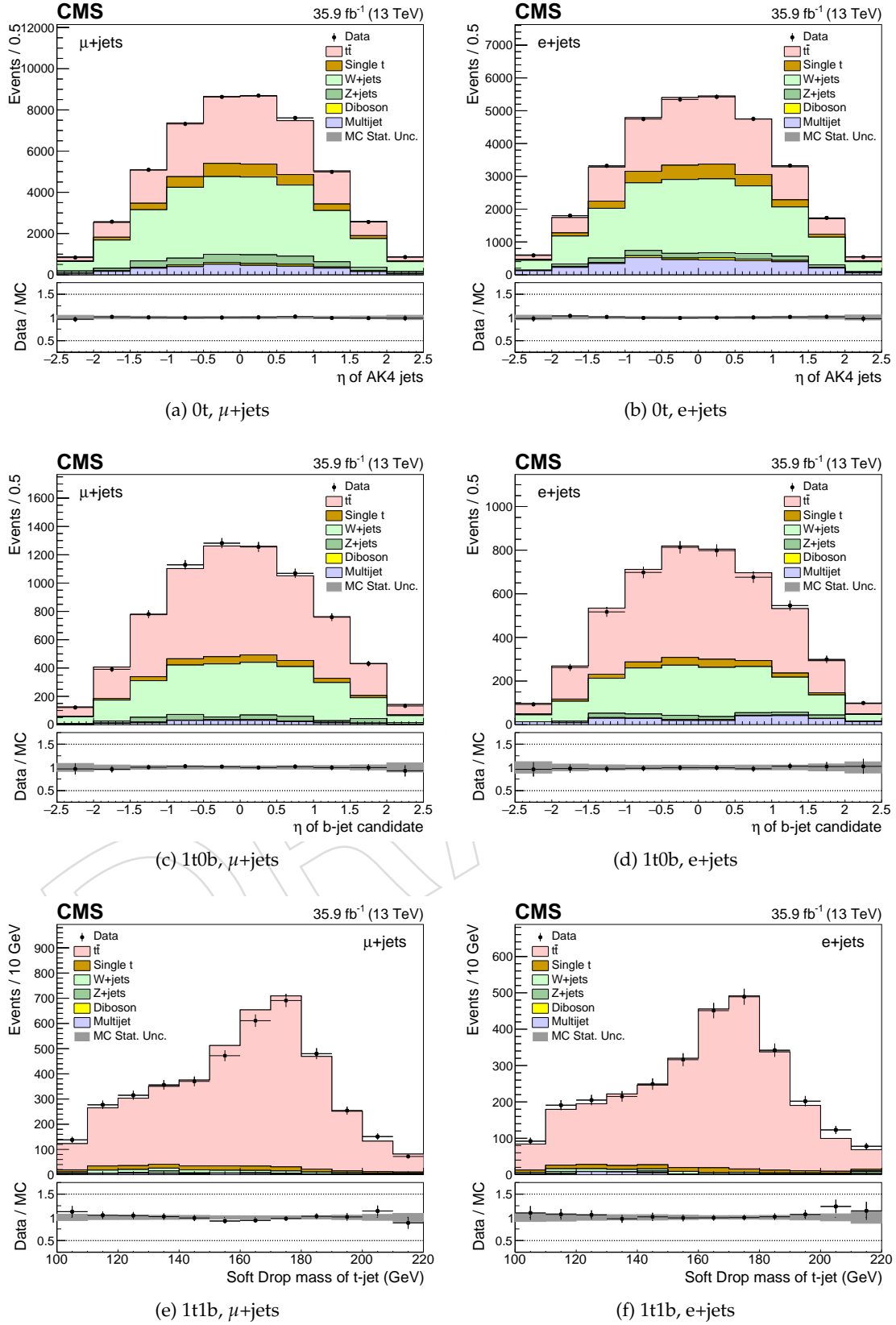


Figure 6: Posterior kinematic distributions for the maximum likelihood fit. Six different event categories are used: (top) 0t, (middle) 1t0b, and (bottom) 1t1b events, in the (top)  $\mu$ +jets and (right) e+jets channel.



336 Figure 7 shows the  $p_T$  and  $y$  distributions for the  $t$  jet candidate in each of the three kinematic  
337 regions for the combined lepton+jets channel. These distributions use the posterior  $t$  tagging  
338 scale factor and background normalizations, but not the posterior values of other nuisance  
339 parameters.

340 The posterior signal strength as determined in the fit is  $0.77 \pm 0.06$ , i.e. the  $t\bar{t}$  simulation is  
341 observed to overestimate the data by roughly 20%. Although the measured signal strength  
342 extrapolated from the fit is not directly used to compute an integrated cross section, it serves as  
343 an indicator of the level of agreement between the measured inclusive  $t\bar{t}$  cross section and the  
344 prediction from simulation in the boosted regime.

DRAFT

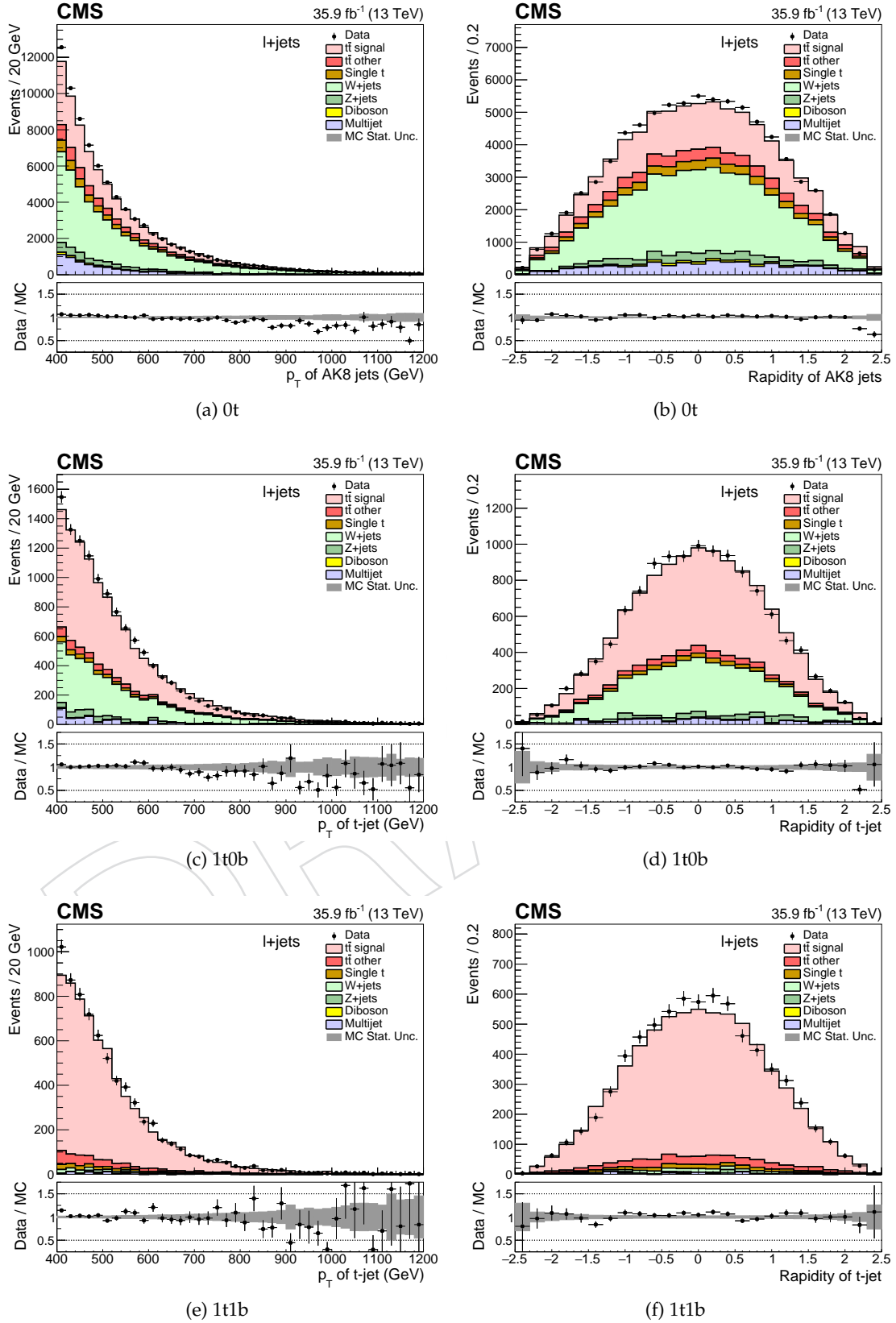


Figure 7: Distributions of the (left)  $p_T$  and (right)  $y$  of the  $t$  jet candidate for the (top)  $0t$ , (middle)  $1t0b$ , and (bottom)  $1t1b$  regions, for events in the combined lepton+jets channel. Posterior  $t$  tag scale factor and background normalizations are used.

## 8 Systematic uncertainties

The systematic uncertainties considered in this analysis pertain from both experimental and theoretical sources. The former includes all uncertainties related to the differences in the object performance between data and simulation, as well as the background modeling. The latter are related to the simulation itself and affect primarily the unfolded results through the acceptance, efficiency, and migration matrices. For each systematic variation, described in detail below, the differential cross sections are re-measured and the difference with respect to the nominal result is taken as the effect of this variation on the measurement.

A number of experimental uncertainty affect the measurement. The dominant uncertainties in the hadronic channel are due to the jet energy scale and the subjet  $b$  tagging efficiency. In the  $l$ +jets channel, the  $t$  tagging and  $b$  tagging efficiency uncertainties result in the largest contributions. The different sources are described in detail in the list below.

- *QCD multijet background (hadronic)*: The fitted QCD yield uncertainty is used. The impact of the shape uncertainties from the closure test in the simulation and the different pileup profiles in the control and signal regions are of the order of 1%.
- *Subdominant backgrounds (hadronic)*: The expected yield of the subdominant background processes estimated from the simulation (single top quark production and vector bosons produced in association with jets) is varied by 50%, leading to a negligible uncertainty (smaller than 1%).
- *Background estimate ( $l$ +jets)*: An a priori uncertainty of 30% is applied to the single top quark and  $W$ +jets background normalizations. An additional uncertainty in the flavor composition of the  $W$ +jets is considered, allowing the light- and heavy-flavor components to vary separately with a 30% normalization uncertainty. For the QCD multijet normalization, a 50% uncertainty is used to reflect the combined uncertainty in the normalization and the extraction of the kinematic distributions from the data sideband region. These are all constrained in the maximum likelihood fit.
- *Jet energy scale*: The uncertainty in the energy scale of each reconstructed large- $R$  jet, the jet energy scale (JES) uncertainty, is a leading experimental uncertainty for the hadronic channel. It is divided in 24 independent sources [45] and treated as follows: for each variation a new jet collection is created and the event interpretation is repeated. This results not only in variations of the  $p_T$  scale itself, but may also lead to different top jet candidates. The JES uncertainty, per jet, is of the order  $1 - 2\%$ ,  $p_T$  and  $\eta$  dependent. The effect on the measured cross section is typically of the order 10% but it can be much larger at high top  $p_T$ . For the  $l$ +jets channel, the jet energy scale uncertainty is estimated for both small- $R$  and large- $R$  jets by shifting the jet energy in simulation up and down by their  $p_T$  and  $\eta$  dependent uncertainties of  $X$ - $Y\%$ .
- *Jet energy resolution*: The impact on the measurement due to the jet energy resolution (JER) is determined by smearing the jets according to the JER uncertainty. The effect on the cross section is relatively small, at the level of 2%.
- *$t$  tagging efficiency ( $l$ +jets)*: The  $t$  tagging efficiency and its associated uncertainty is simultaneously extracted with the signal strength and background normalizations in the likelihood fit for the  $l$ +jets analysis. This is described in Section 7.
- *Subjet  $b$  tagging efficiency (hadronic)*: The uncertainty in the identification of  $b$ -subjets within the large- $R$  jets is a leading experimental uncertainty in the hadronic channel. The effect on the cross sections is of the order of 10% relatively flat in all the

observables. Unlike the uncertainty associated with the JES, the b-subjet tagging uncertainty therefore largely cancels in the normalized cross sections.

- *b tagging efficiency (l+jets)*: For the l+jets channel, the small- $R$  jet b tagging efficiency observed in the simulation is corrected to match that in data using  $p_T$  and  $\eta$  dependent scale factors [52]. The corresponding uncertainty varies between about X–Y%. The b tagging efficiency and light jet misidentification rates are treated as fully correlated.
- *Pileup*: The uncertainty related to the modeling of additional pileup interactions is a subdominant uncertainty. The impact on the measurement is estimated by varying the total inelastic cross section used to weight the simulated events by  $\pm 4.6\%$ . The effect on the cross sections is negligible (below 1%).
- *Trigger (hadronic)*: The uncertainty associated with the trigger, accounting for the difference between the simulated and observed trigger efficiency, is well below 1% in the phase space for the hadronic channel.
- *Lepton identification and trigger (l+jets)*: The performance of the lepton identification, reconstruction, trigger, and isolation provides a small source of uncertainty. Correction factors used to modify the simulation to match the efficiencies observed in data are estimated with a tag-and-probe method using  $Z \rightarrow \ell\ell$  decays. The corresponding uncertainty is determined by varying the correction factors up or down within their uncertainties. The resulting uncertainty for muons and electrons are XX% and YY%, respectively.
- *Luminosity*: The uncertainty in the measurement of the integrated luminosity is 2.5% [55].

The theoretical uncertainties are divided into two sub-categories: the ones related to the matrix element of the hard scatter process and the ones related to the modeling of the parton shower and the underlying event. The first category (consisting of the first three sources below) is evaluated by variations of the simulated event weights, while the second category is evaluated with dedicated, alternative Monte Carlo samples with modified parameters.

- *Parton distribution functions*: The uncertainty due to parton distribution functions (PDFs) is estimated by applying event weights corresponding to the 100 replicas of the NNPDF set. For each observable we compute its standard deviation from the 100 variations.
- *Renormalization and factorization scales*: This source of systematic uncertainty is estimated by applying event weights corresponding to different factorization and renormalization scale options. For each observable the largest deviation from the nominal scales is taken.
- *Strong coupling constant ( $\alpha_s$ )*: The uncertainty associated with the  $\alpha_s$  is estimated by applying event weights corresponding to higher and lower values of  $\alpha_s$  for the matrix element.
- *Final and initial state radiation*: The uncertainty in the initial state radiation (ISR) and the final state radiation (FSR) is estimated from alternative Monte Carlo samples with reduced and increased value for the strong coupling constant used by PYTHIA to generate final/initial state radiation.
- *Matrix element – parton shower matching*: In the POWHEG matrix element to parton shower (ME-PS) matching scheme, the resummation damping factor  $h_{\text{damp}}$  is used to regulate high- $p_T$  radiation. Uncertainties in  $h_{\text{damp}}$  are parameterized by considering

alternative simulated samples with  $h_{\text{damp}}$  varied by  $\pm 1\sigma$ .

- *Underlying event tune:* This uncertainty is estimated from alternative Monte Carlo samples with the tune CUETP8M2T4 parameters varied by  $\pm 1\sigma$ .

## 9 Cross section measurements

This section discusses the differential cross section measurements for the hadronic and lepton+jets channels.

### 9.1 Definition of particle and parton level

The partonic phase space to which the measurement is unfolded is constrained by the kinematic requirements of the detector-level fiducial region. Namely, for the hadronic channel, the top and anti-top partons must have  $p_T > 400$  GeV and  $|\eta| < 2.4$ , while the invariant mass of the  $t\bar{t}$  system must be greater than 800 GeV in order to avoid extreme events with high top  $p_T$  and very low  $m_{t\bar{t}}$ .

For the lepton+jets channel, the parton level definition is different from the hadronic channel because the differential cross section is reported as a function of the hadronically decaying top quark. Therefore, the parton level phase space is confined to semileptonic events, where the  $p_T$  of the hadronically decaying top quark is greater than 400 GeV, to match the fiducial requirement at detector level.

The so-called *particle level* represents the state that consists of stable particles originating from the proton-proton collision, after the hadronization process, and before the interaction of these particles with the detector. The observables computed from the particles' momenta are thought to be better defined compared to the ones computed from parton information. Also, the associated phase space is closer to the fiducial phase space of the measurement at detector level, which results in smaller theoretical uncertainties. In the context of this analysis, particle jets are reconstructed from stable particles, excluding neutrinos, with the anti- $k_T$  algorithm of distance parameter 0.8, identical to the detector-level reconstruction. It should be noted that only particles originating from the primary interaction are considered. Subsequently, jets that are geometrically matched, within  $\Delta R < 0.4$  in  $\eta - \phi$  from generated leptons (i.e. from the leptonic decays of the W boson) are removed from the particle jet collection. Finally, the two particle jets with the highest  $p_T$  are considered the particle-level top-quark candidates for the hadronic channel. In order to match as closely as possible the fiducial phase space, the same kinematic cuts are applied as for detector-level events. In particular, the particle jets must have  $p_T > 400$  GeV and  $|\eta| < 2.4$ , while the mass of each jet should be in the range 120–220 GeV and the invariant mass of the two jets greater than 800 GeV. The matching efficiency between the particle-level top-quark candidates and the original top quarks at parton level varies between 96% and 98%.

The particle level phase space for the lepton+jets channel is set up to mimic the kinematic selections at reconstructed level. Particle-level large- $R$  jets are selected if they fulfill  $p_T > 400$  GeV,  $|\eta| < 2.4$ , and  $105 < m_{\text{jet}} < 220$  GeV, and are then referred to as particle-level top jets. Particle-level small- $R$  jets are selected if they have  $p_T > 50$  GeV,  $|\eta| < 2.4$ , and are flagged as a b jet), referred to as particle-level b jets. Particle-level electrons (muons) are selected if they have  $p_T > 50$  GeV and  $|\eta| < 2.5(2.1)$ . To fulfill the particle-level selection criteria, an event must contain at least one particle-level top jet, at least one particle-level b jet, and at least one particle-level electron or muon.

The fraction  $f_1$  is defined as the fraction of reconstructed events that have an equivalent event at the unfolded level (parton or particle) in the same observable range, whereas the fraction  $f_2$  is the fraction of events at the unfolded level that have an equivalent reconstructed event. Figures 8 and 9 show the aforementioned fractions at parton and particle level, respectively, for the hadronic channel as a function of (inclusive) top  $p_T$  and  $\eta$ . The  $f_1$  vs  $p_T$  shows a characteristic threshold behavior due to the finite  $p_T$  resolution, while it is flat vs  $\eta$ . The  $f_2$  decreases vs  $p_T$ , primarily due to the subjet b tagging inefficiency and the NN output dependence on the  $p_T$  (at high jet  $p_T$  it is more difficult to differentiate between ordinary QCD jets and boosted tops). Also, the  $f_2$  decreases at high  $|\eta|$  values due to the increased b tagging inefficiency at the edges of the CMS tracker subdetector.

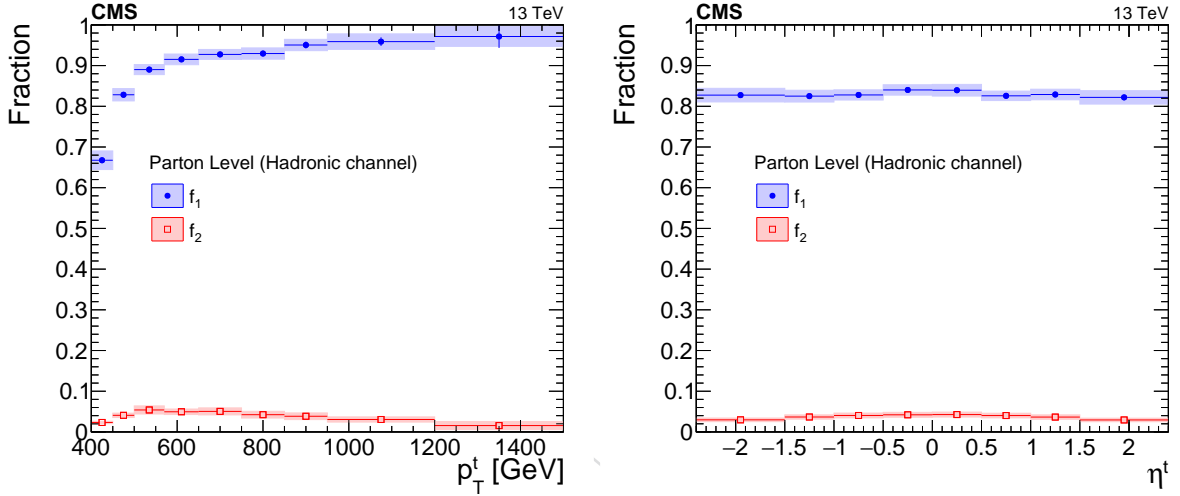


Figure 8: Simulated fractions  $f_{1,2}$  for the parton-level selection in the hadronic channel as a function of (inclusive) top  $p_T$  and  $\eta$ .

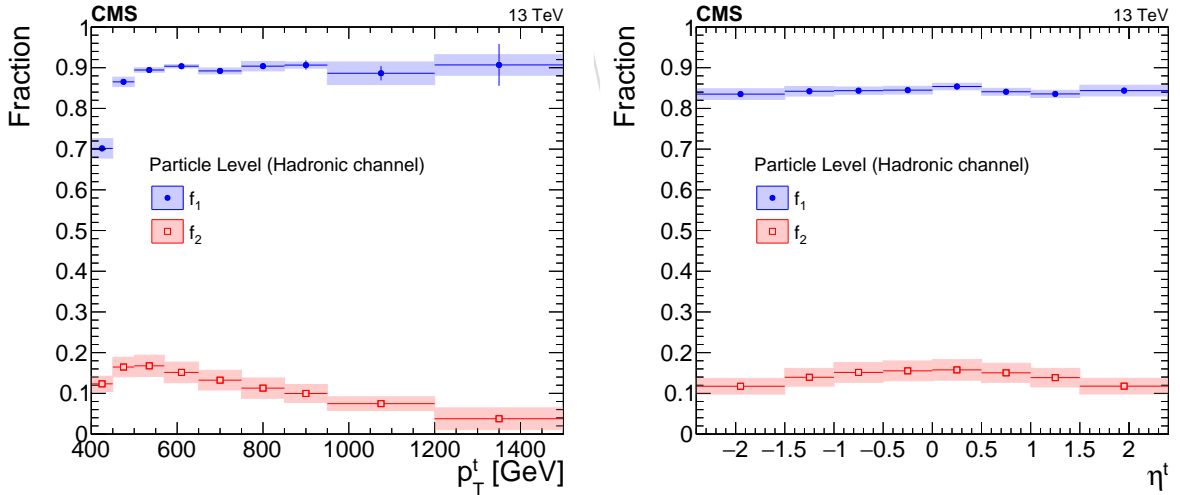


Figure 9: Simulated fractions  $f_{1,2}$  for the particle-level selection in the hadronic channel as a function of (inclusive) top  $p_T$  and  $\eta$ .

## 9.2 Unfolding

The unfolded cross sections are extracted according to Eq. 4:

$$\frac{d\sigma_i^{\text{unf}}}{dx} = \frac{1}{\mathcal{L} \cdot \Delta x_i} \cdot \frac{1}{f_{2,i}} \cdot \sum_j \left( R_{ij}^{-1} \cdot f_{1,j} \cdot S_j \right), \quad (4)$$

where  $\mathcal{L}$  is the total integrated luminosity and  $\Delta x_i$  is the width of the  $i$ -th bin of the observable  $x$ . The quantity  $R_{ij}^{-1}$  is the inverse of the migration matrix between the  $i$ -th and  $j$ -th bins. Due to the finite resolution of the detector, the migration matrix is non-diagonal and thus the application of an unfolding procedure is necessary. The binning of the various observables has been chosen such that the purity (fraction of reconstructed events that the true value of the observable lies in the same bin) and the stability (fraction of true events that the reconstructed observable lies in the same bin) are well above 50%. This choice results in highly diagonal migration matrices, shown for the hadronic channel in Figures 10 and 11, and for the lepton+jets channel in Figures 12 and 13. In order to avoid the biases introduced by the various unfolding methods with some type of regularization, the simple migration matrix inversion is used, as written in Eq. 4, at a price of a moderate increase of the statistical uncertainty.

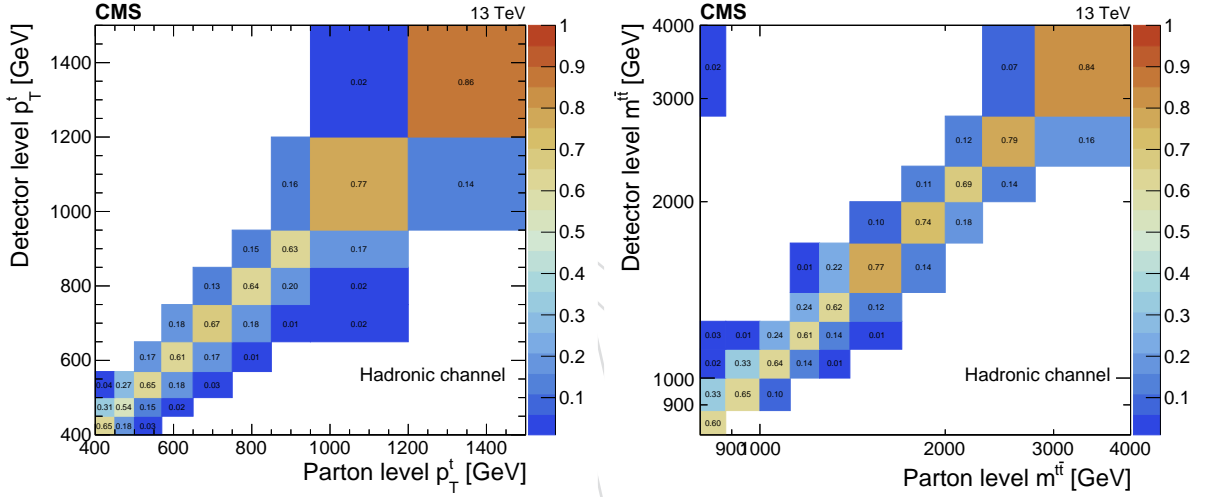


Figure 10: Simulated migration matrices for (inclusive) top  $p_T$  (left) and  $m^{t\bar{t}}$  (right) at parton level in the hadronic channel. Each column is normalized to unity.

### 9.3 Hadronic channel

For the hadronic channel, the measurement of the differential cross sections are performed at the detector level and subsequently they are reported at the parton and particle levels.

#### 9.3.1 Fiducial cross sections at detector level

The fiducial differential cross section is derived in bin  $i$  of the variable  $x$  from the signal yield  $S_i$  (eq. 2) in the bin as follows:

$$\frac{d\sigma_i^{\text{fid}}}{dx} = \frac{S_i}{\mathcal{L} \cdot \Delta x_i}, \quad (5)$$

where  $\mathcal{L}$  is the total integrated luminosity. Of particular interest is also the normalized cross section, computed as:



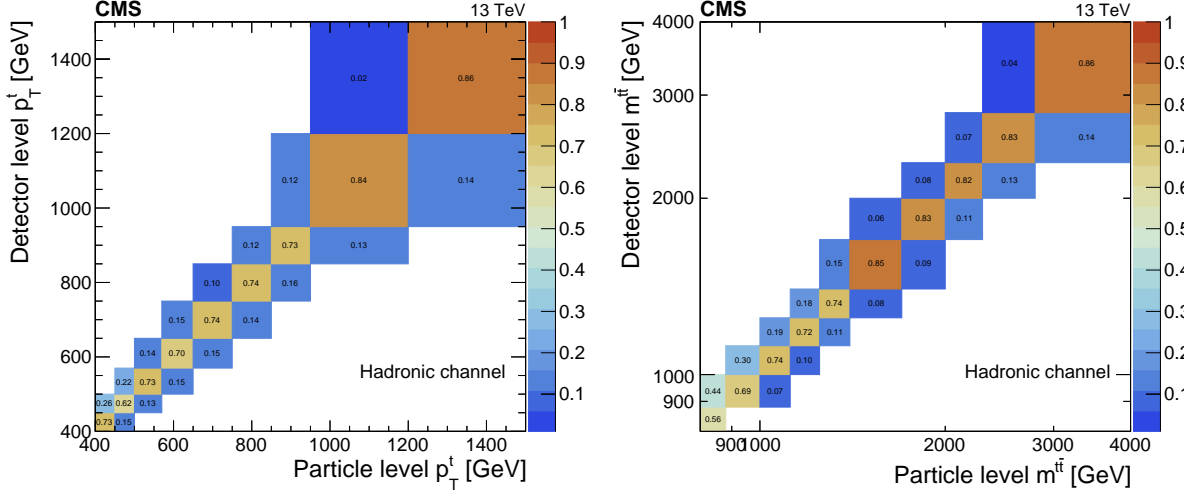


Figure 11: Simulated migration matrices for (inclusive) top  $p_T$  (left) and  $m^{t\bar{t}}$  (right) at particle level in the hadronic channel. Each column is normalized to unity.

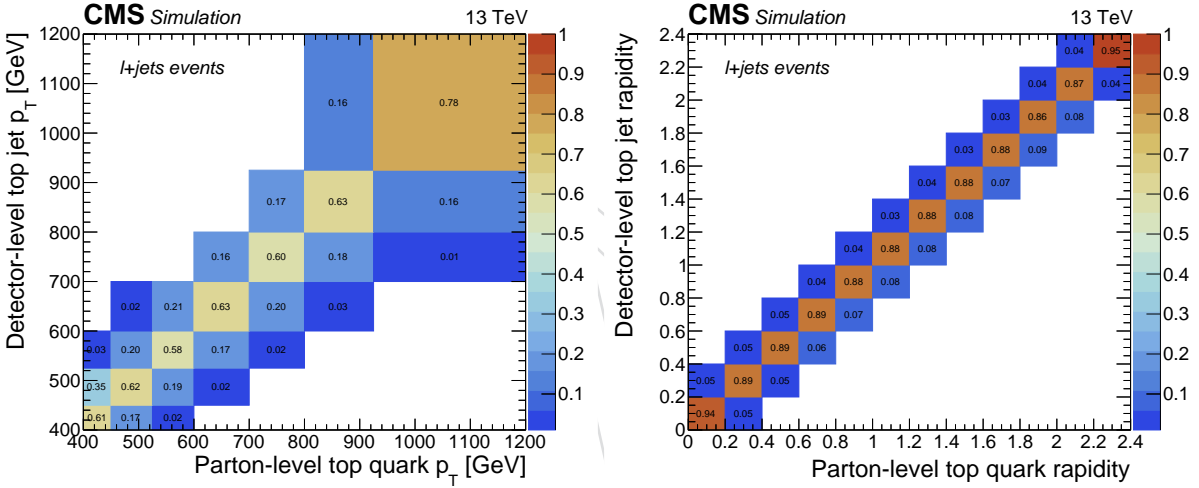


Figure 12: Simulated migration matrices for top quark  $p_T$  (left) and rapidity (right) at parton level in the lepton+jets channel. Each row is normalized to unity.

$$\frac{1}{\sigma^{\text{fid}}} \frac{d\sigma_i^{\text{fid}}}{dx} = \frac{1}{\sum_k S_k} \cdot \frac{S_i}{\mathcal{L} \cdot \Delta x_i}, \quad (6)$$

which is used to confront the modeling of the differential cross section regardless of the overall normalization. In order to estimate the uncertainty in the measurement, the entire procedure is repeated for every source of uncertainty. Both the experimental and the theoretical uncertainties affect primarily the  $t\bar{t}$  signal shape, which is used to fit the data for the QCD background normalization. As a result the total systematic uncertainty of the measurement is small and the statistical uncertainty dominates. This is true both for the absolute and the normalized cross sections.

### 9.3.2 Particle-level fiducial cross sections

The unfolded cross sections (see Section 9.2) are shown in Figs. 14- 18. Firstly, the expected offset of about 40% in the total cross section between the data and the POWHEG +PYTHIA pre-

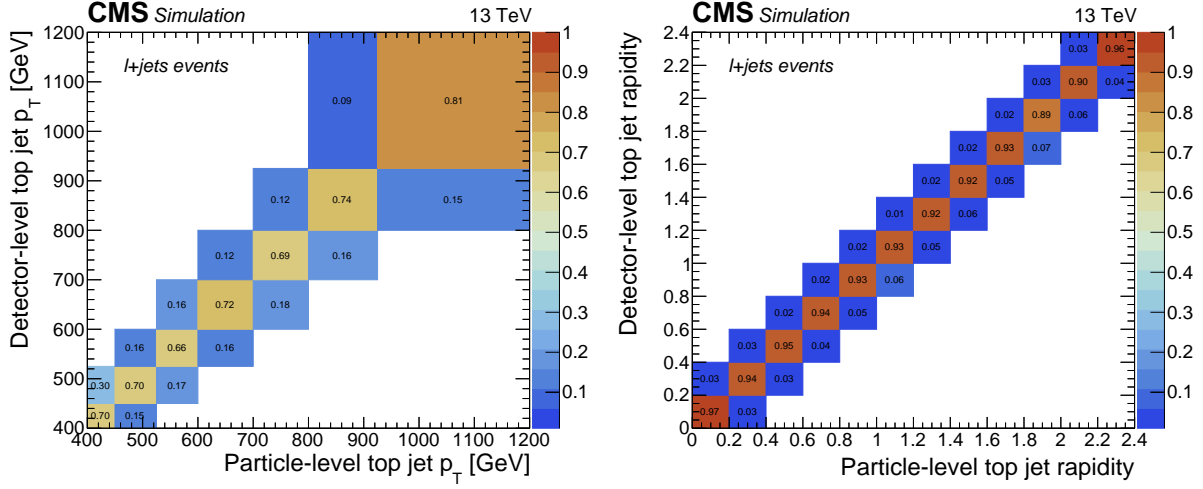


Figure 13: Simulated migration matrices for top jet  $p_T$  (left) and rapidity (right) at particle level in the lepton+jets channel. Each row is normalized to unity.

521 diction is observed, which is considerably smaller for the other theory predictions. In terms of  
 522 shape comparisons, the POWHEG +PYTHIA prediction is in excellent agreement with data for all  
 523 the variables, except for the invariant mass  $m^{t\bar{t}}$  of the  $t\bar{t}$  system, where the theoretical spectrum  
 524 appears to be harder above  $\approx 2$  TeV. A similar behavior is observed for the other theory models  
 525 too, although the precision of the measurement does not allow quantitative comparisons.

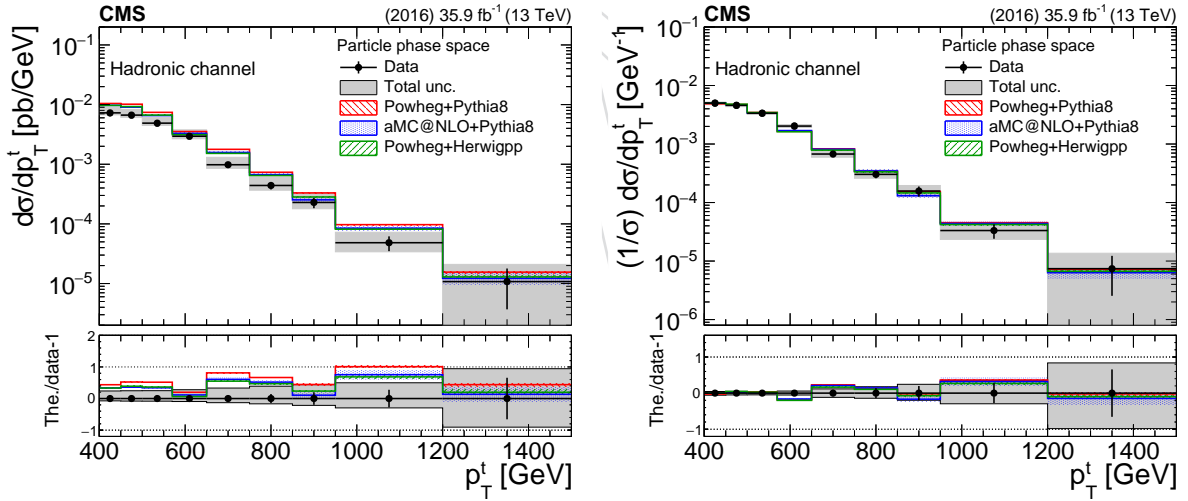


Figure 14: Differential cross section unfolded to particle level, absolute (left) and normalized (right), as a function of (inclusive) top  $p_T$  in the hadronic channel. The bottom panel shows the ratio (theory - data)/data.

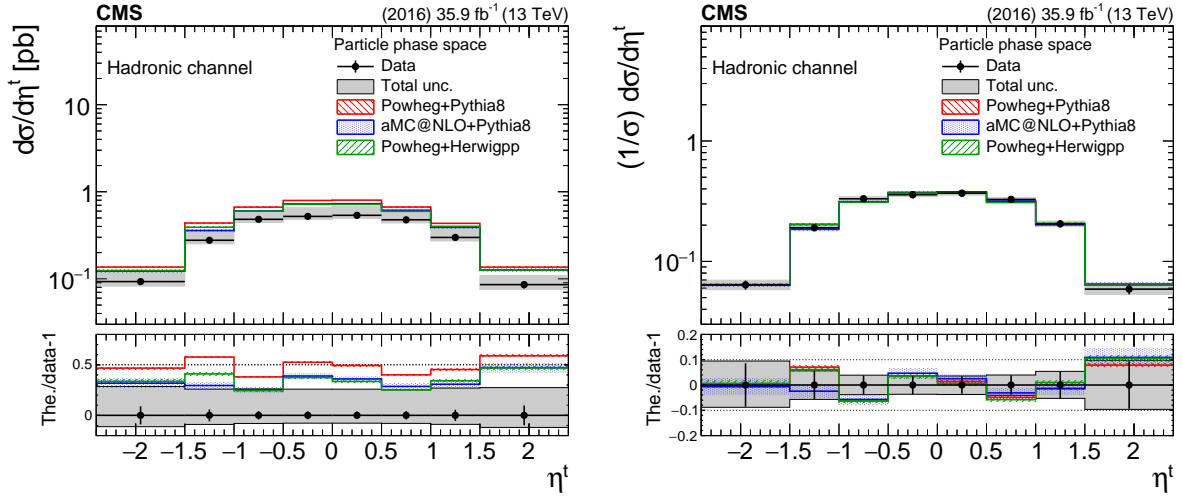


Figure 15: Differential cross section unfolded to particle level, absolute (left) and normalized (right), as a function of (inclusive) top  $\eta$  in the hadronic channel. The bottom panel shows the ratio (theory - data)/data.

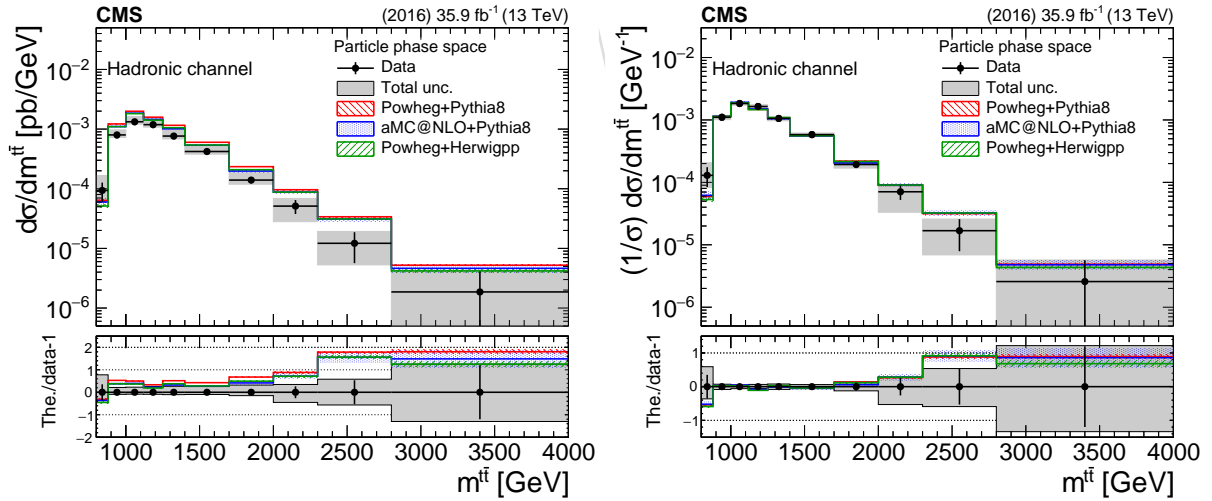


Figure 16: Differential cross section unfolded to particle level, absolute (left) and normalized (right), as a function of  $m^{t\bar{t}}$  in the hadronic channel. The bottom panel shows the ratio (theory - data)/data.

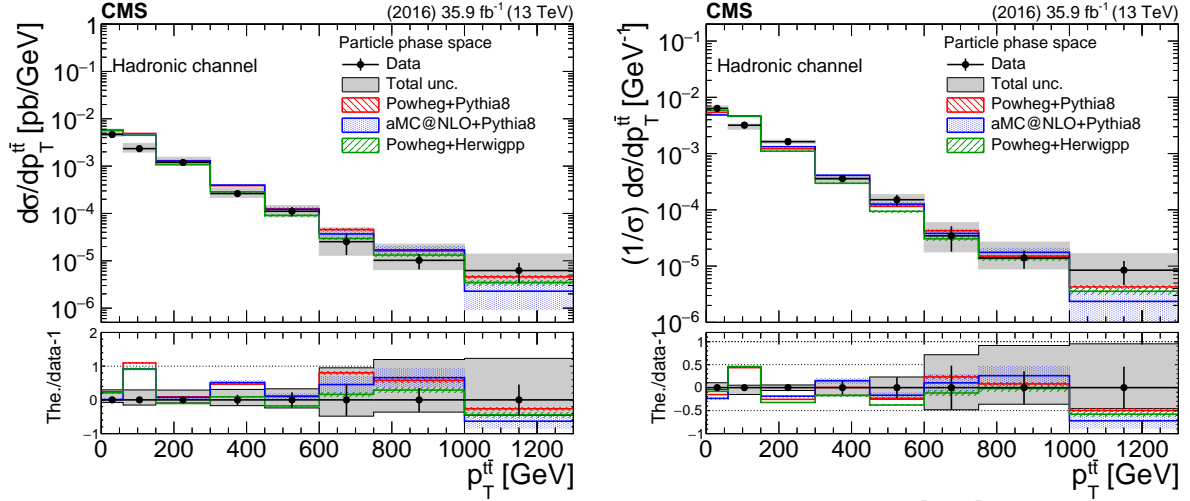


Figure 17: Differential cross section unfolded to particle level, absolute (left) and normalized (right), as a function of  $p_T^{t\bar{t}}$  in the hadronic channel. The bottom panel shows the ratio (theory - data)/data.

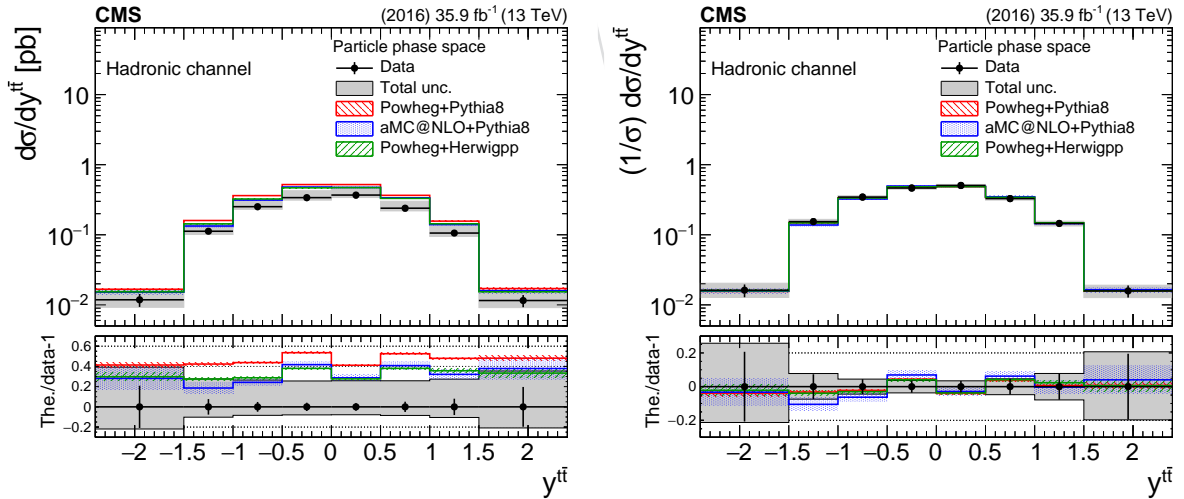


Figure 18: Differential cross section unfolded to particle level, absolute (left) and normalized (right), as a function of  $y^{t\bar{t}}$  in the hadronic channel. The bottom panel shows the ratio (theory - data)/data.

## 526 9.3.3 Parton-level cross sections

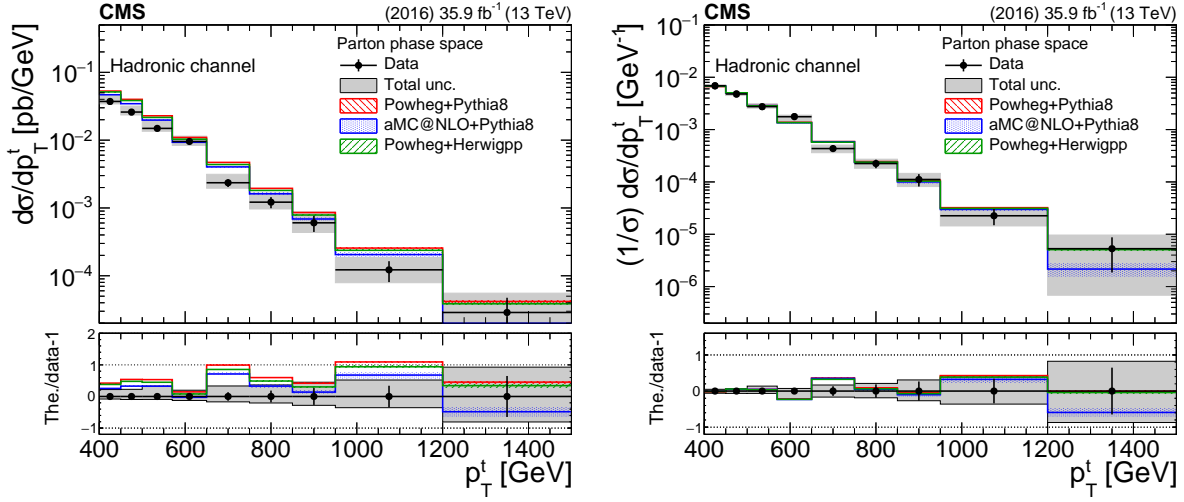


Figure 19: Differential cross section unfolded to parton level, absolute (left) and normalized (right), as a function of (inclusive) top  $p_T$  in the hadronic channel. The bottom panel shows the ratio (theory - data)/data.

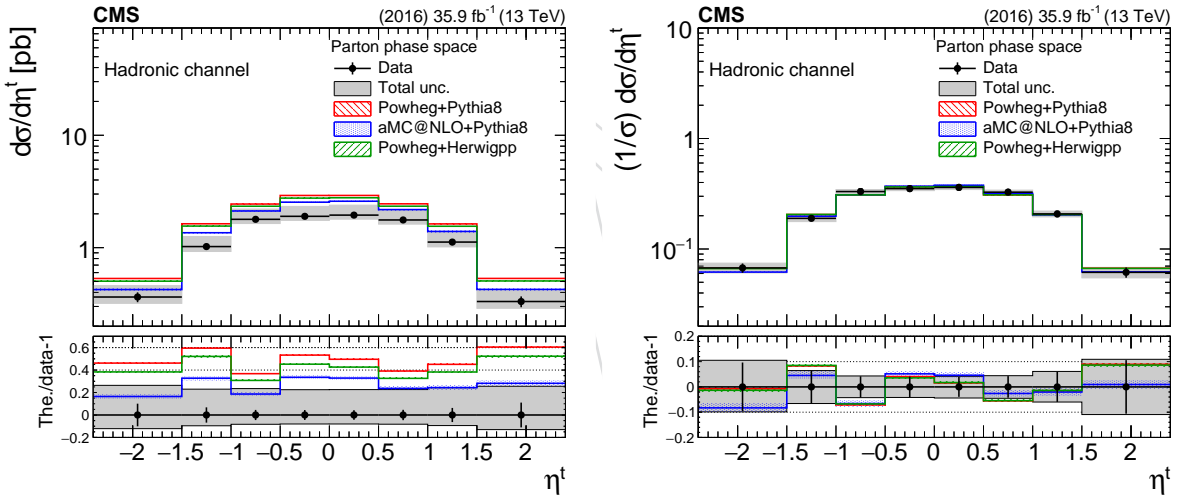


Figure 20: Differential cross section unfolded to parton level, absolute (left) and normalized (right), as a function of (inclusive) top  $\eta$  in the hadronic channel. The bottom panel shows the ratio (theory - data)/data.

527 Figure 24 shows a summary of the systematic uncertainties on the differential cross sections at  
 528 parton and particle level as a function of top  $p_T$ .

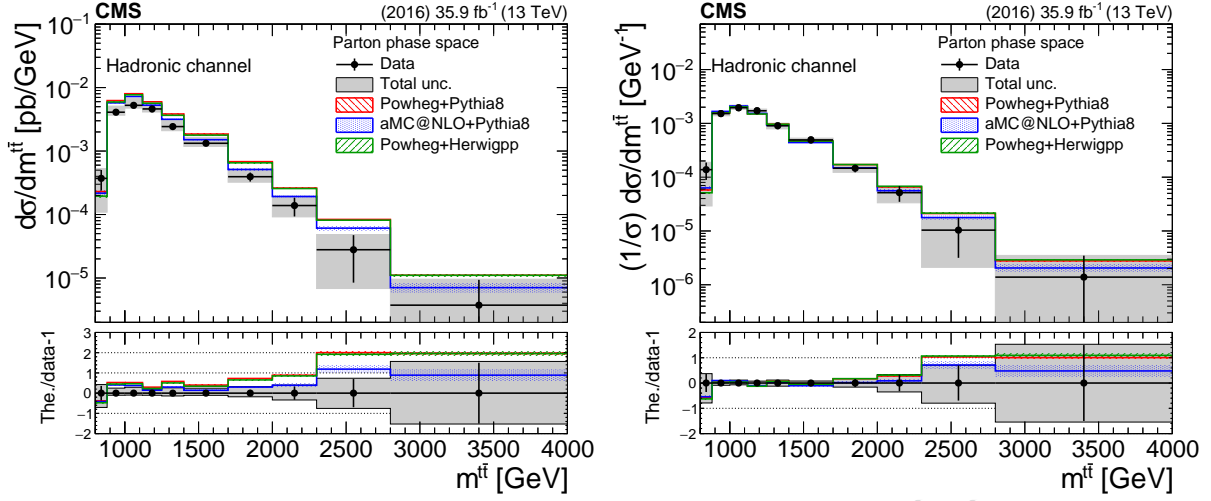


Figure 21: Differential cross section unfolded to parton level, absolute (left) and normalized (right), as a function of  $m_{t\bar{t}}$  in the hadronic channel. The bottom panel shows the ratio (theory - data)/data.

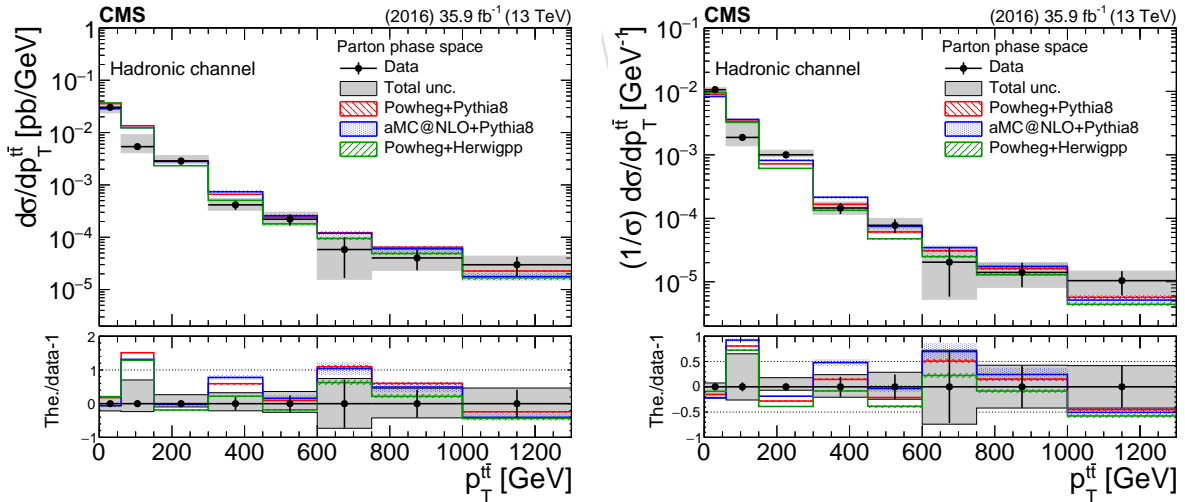


Figure 22: Differential cross section unfolded to parton level, absolute (left) and normalized (right), as a function of  $p_T^{t\bar{t}}$  in the hadronic channel. The bottom panel shows the ratio (theory - data)/data.

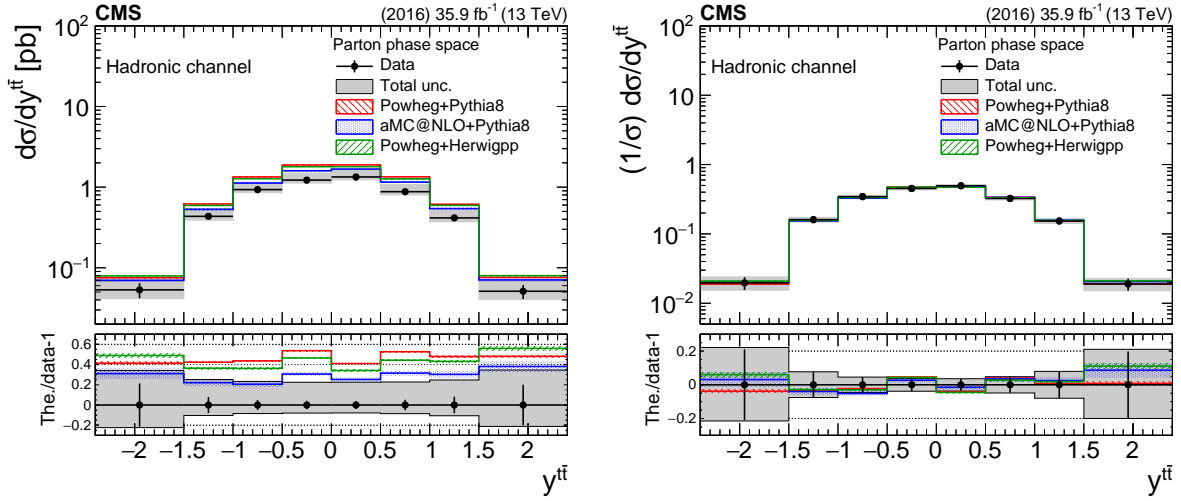


Figure 23: Differential cross section unfolded to parton level, absolute (left) and normalized (right), as a function of  $y^{t\bar{t}}$  in the hadronic channel. The bottom panel shows the ratio (theory - data)/data.

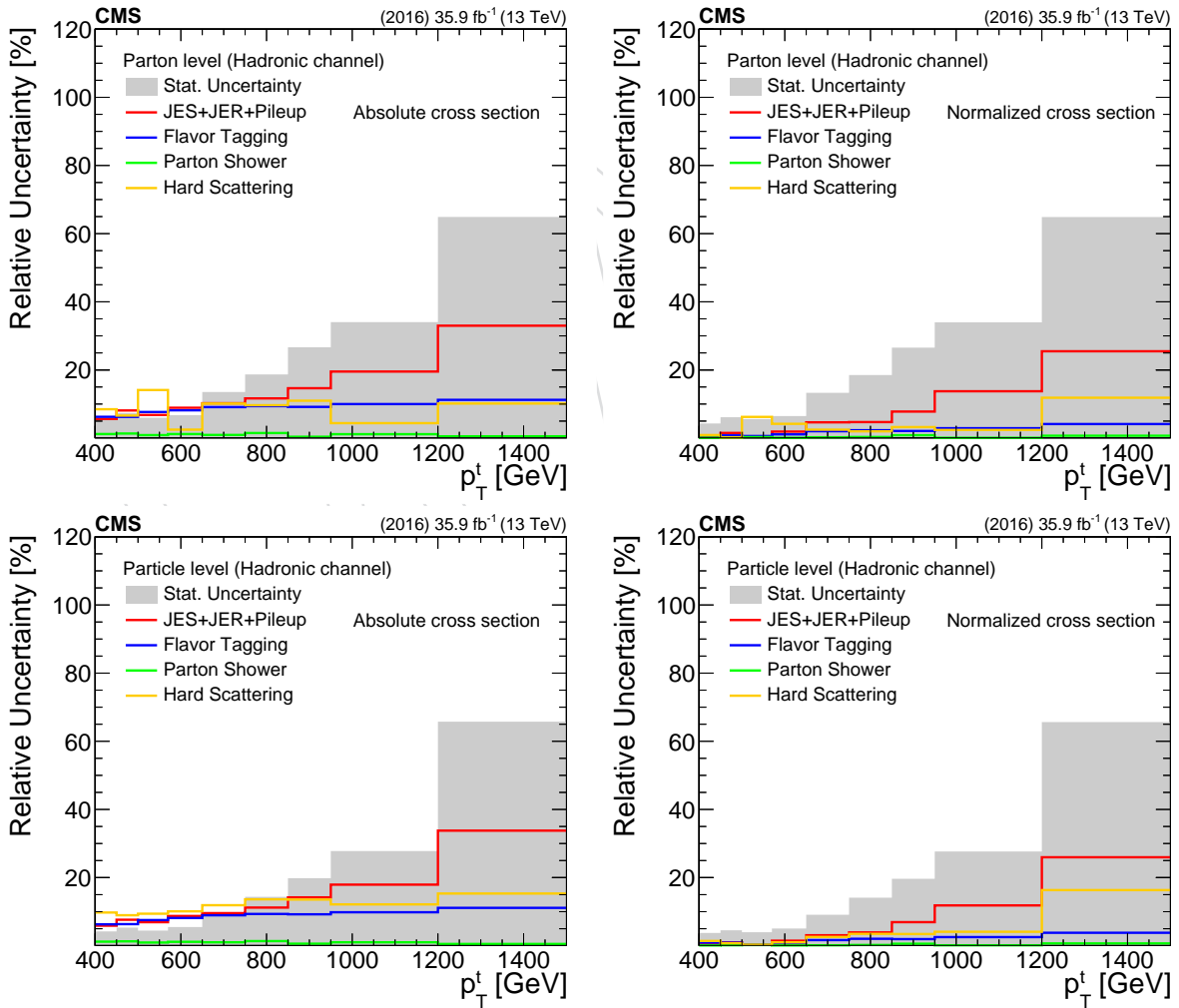


Figure 24: Decomposition of uncertainties for the parton- and particle-level measurement (left: absolute, right: normalized) as a function of (inclusive) top  $p_T$  in the hadronic channel.



## 9.4 Lepton+jets channel

The differential  $t\bar{t}$  cross section is measured as a function of the  $p_T$  and  $y$  of the hadronically-decaying top quark. The measurement is performed at particle level within a region of phase space following the event selection criteria, as well as at parton level within the full phase space. Semi-leptonic  $t\bar{t}$  events are selected at parton level, and the properties of the hadronically-decaying top quark is used as the true top quark  $p_T$ .

The differential cross section is extracted from the signal-dominated 1t1b category. The measured signal distribution is determined by subtracting the estimated background contributions from the distribution in data, using the posterior normalizations from the fit given in Table 1. To account for signal reconstruction efficiencies and bin migrations, an unfolding procedure based on a least squares minimization with Tikhonov regularization, as implemented in the TUNFOLD framework, is applied [56]. A non-regularized unfolding is chosen to be optimal for the measurement. The unfolding relies on response matrices that map the  $p_T$  and  $y$  distributions for the  $t$  tagged jet to corresponding properties for either the particle-level  $t$  jet candidate or the parton-level top quark.

The systematic uncertainty in the unfolded measurement receives contributions from experimental and theoretical sources, discussed in Section 8. The posteriori values from the likelihood fit are used for the  $t$  tagging efficiency, background normalizations, and lepton efficiencies, while the a priori values are used for the remaining uncertainties. For each systematic variation that affects the shape of the  $p_T$  or  $y$  distribution, a separate response matrix is created that is used to unfold the data. The resulting uncertainties are added in quadrature to obtain the total uncertainty for the unfolded distribution. The theoretical and experimental uncertainties are accounted for separately.

The muon and electron channels are combined before the unfolding, by merging the measured muon and electron distributions as well as the response matrices. The background contributions are also merged before subtracting these from the measured distributions, with the exception of the muon and electron multijet backgrounds that are treated as separate background sources.

The unfolded results are shown in Figure 25 and the normalized unfolded cross section results are shown in Figure 26. The measurements are compared to the prediction from POWHEG +PYTHIA 8. The breakdown of the sources of systematic uncertainty are shown in Figure 27.

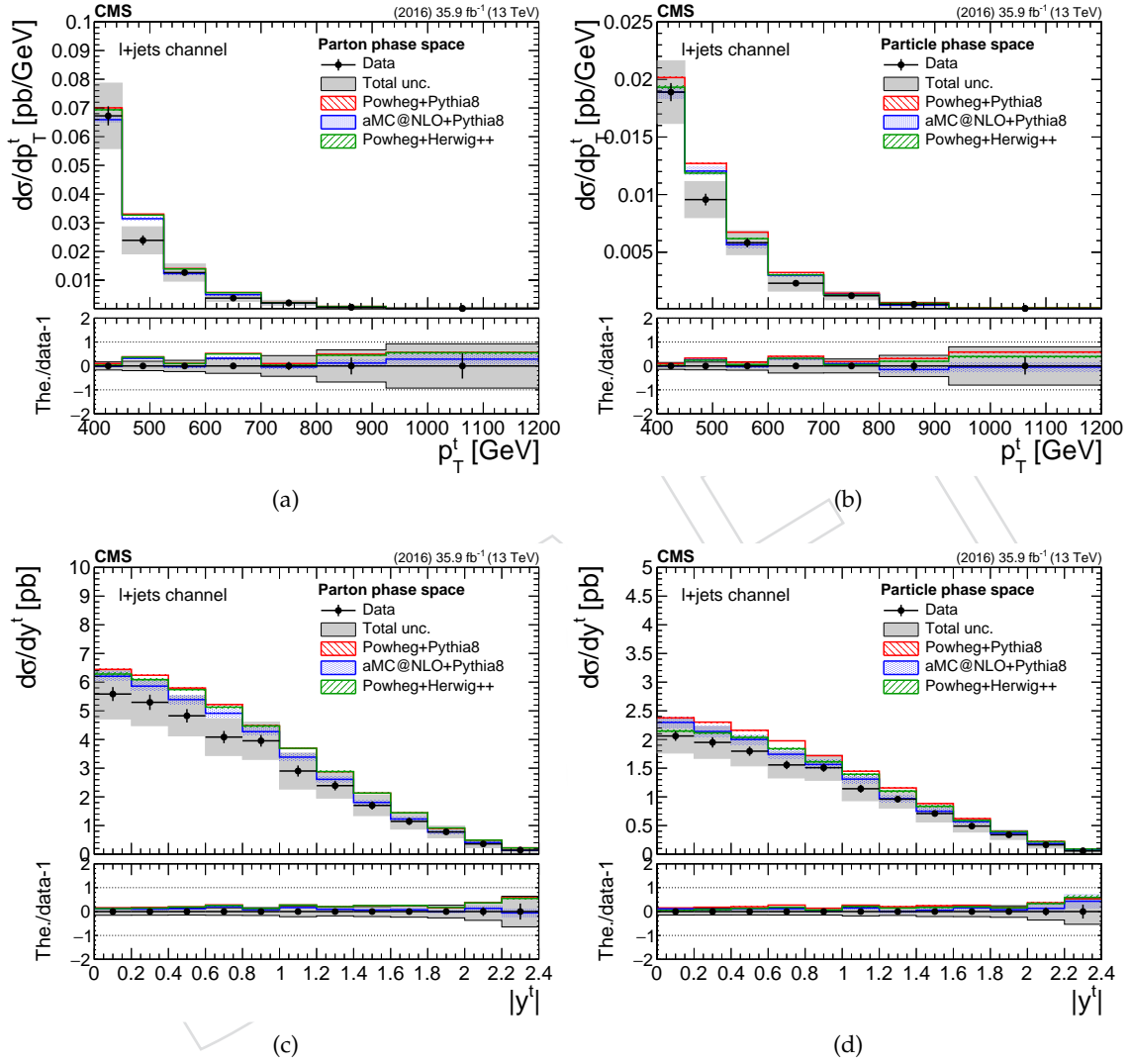


Figure 25: Differential cross section measurement at parton level (top row) as a function of the top quark  $p_T$  (top left) and rapidity (top right), and at particle level (bottom row) as a function of the particle-level t jet  $p_T$  (bottom left) and rapidity (bottom right) for the lepton+jets analysis.

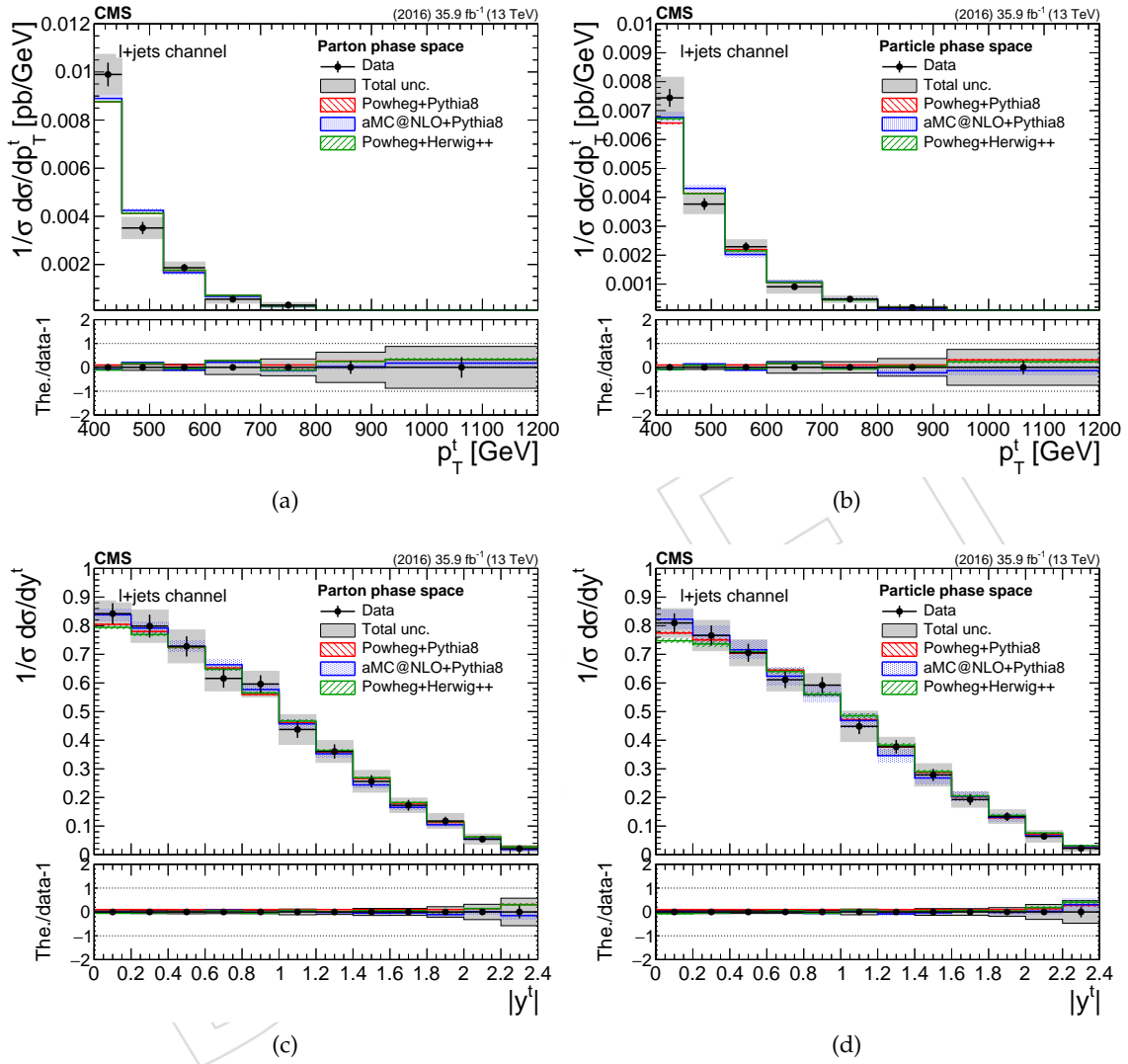


Figure 26: Normalized differential cross section measurement at parton level (top row) as a function of the top quark  $p_T$  (top left) and rapidity (top right), and at particle level (bottom row) as a function of the particle-level t jet  $p_T$  (bottom left) and rapidity (bottom right) for the lepton+jets analysis.

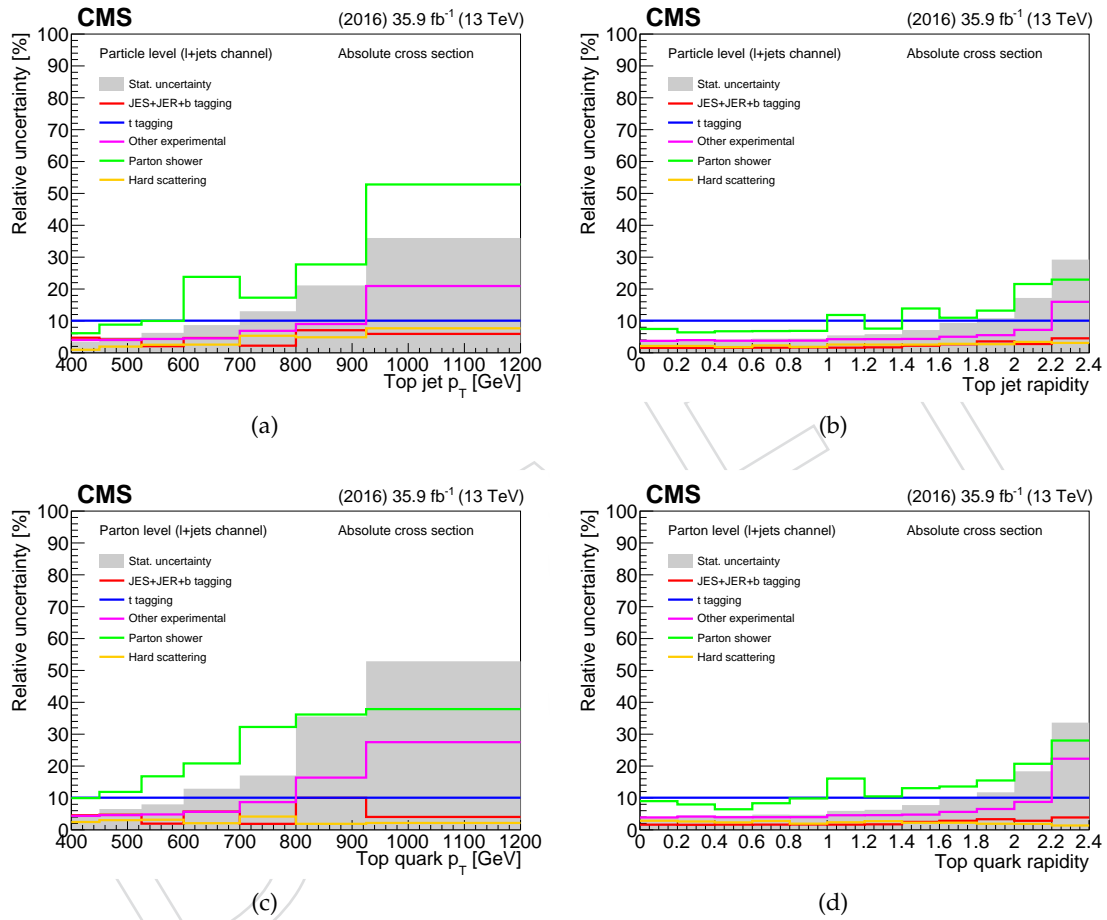


Figure 27: Breakdown of sources of systematic uncertainty affecting the differential cross section measurements in the lepton+jets analysis at particle level (top row) and at parton level (bottom row).

## 10 Summary

A measurement of the  $t\bar{t}$  production cross section for high- $p_T$  top quarks at 13 TeV proton-proton collisions has been presented. The measurement is performed with events where either one or both top quarks decay hadronically, and where the hadronic decay products cannot be resolved but are instead clustered in a single large- $R$  jet with  $p_T > 400$  GeV. The hadronic final state thus contains two large- $R$  jets, while the lepton+jets final state is identified through the presence of an electron/muon, a  $b$  tagged jet from the leptonically decaying top quark, missing transverse momentum from the escaping neutrino, and a single  $t$  tagged large- $R$  jet. The cross section is reported differentially, for the hadronic channel, as a function of (inclusive) top  $p_T$  and  $\eta$ , and as a function of the invariant mass,  $p_T$ , and rapidity of the  $t\bar{t}$  system, unfolded to the parton and particle levels, absolute and normalized. For the lepton+jets channel, the differential cross section is measured as a function of the  $p_T$  and  $y$  of the hadronically decaying top quark, at particle level within a fiducial phase space and at parton level. The results are compared to theoretical predictions from the POWHEG matrix-element generator, interfaced with PYTHIA 8 or HERWIG ++ for the underlying event and parton shower, and from the MC@NLO matrix-element generator, interfaced with PYTHIA 8. All the models overpredict significantly the absolute cross section in the phase space of the measurement (up to 40%), while they are able to describe consistently the differential shapes in all the variables. The most notable discrepancy can be seen for the hadronic channel in the invariant mass of the  $t\bar{t}$  system, where the theoretical models predict higher cross section at high mass values. However, in order to estimate the significance of the discrepancy, more data are needed.

## Acknowledgements

We congratulate our colleagues in the CERN accelerator departments for the excellent performance of the LHC and thank the technical and administrative staffs at CERN and at other CMS institutes for their contributions to the success of the CMS effort. In addition, we gratefully acknowledge the computing centres and personnel of the Worldwide LHC Computing Grid for delivering so effectively the computing infrastructure essential to our analyses. Finally, we acknowledge the enduring support for the construction and operation of the LHC and the CMS detector provided by the following funding agencies: the Austrian Federal Ministry of Education, Science and Research and the Austrian Science Fund; the Belgian Fonds de la Recherche Scientifique, and Fonds voor Wetenschappelijk Onderzoek; the Brazilian Funding Agencies (CNPq, CAPES, FAPERJ, FAPERGS, and FAPESP); the Bulgarian Ministry of Education and Science; CERN; the Chinese Academy of Sciences, Ministry of Science and Technology, and National Natural Science Foundation of China; the Colombian Funding Agency (COLCIENCIAS); the Croatian Ministry of Science, Education and Sport, and the Croatian Science Foundation; the Research Promotion Foundation, Cyprus; the Secretariat for Higher Education, Science, Technology and Innovation, Ecuador; the Ministry of Education and Research, Estonian Research Council via IUT23-4 and IUT23-6 and European Regional Development Fund, Estonia; the Academy of Finland, Finnish Ministry of Education and Culture, and Helsinki Institute of Physics; the Institut National de Physique Nucléaire et de Physique des Particules / CNRS, and Commissariat à l'Énergie Atomique et aux Énergies Alternatives / CEA, France; the Bundesministerium für Bildung und Forschung, Deutsche Forschungsgemeinschaft, and Helmholtz-Gemeinschaft Deutscher Forschungszentren, Germany; the General Secretariat for Research and Technology, Greece; the National Research, Development and Innovation Fund, Hungary; the Department of Atomic Energy and the Department of Science and Technology, India; the Institute for Studies in Theoretical Physics and Mathematics, Iran; the Science Foundation, Ire-

land; the Istituto Nazionale di Fisica Nucleare, Italy; the Ministry of Science, ICT and Future Planning, and National Research Foundation (NRF), Republic of Korea; the Ministry of Education and Science of the Republic of Latvia; the Lithuanian Academy of Sciences; the Ministry of Education, and University of Malaya (Malaysia); the Ministry of Science of Montenegro; the Mexican Funding Agencies (BUAP, CINVESTAV, CONACYT, LNS, SEP, and UASLP-FAI); the Ministry of Business, Innovation and Employment, New Zealand; the Pakistan Atomic Energy Commission; the Ministry of Science and Higher Education and the National Science Centre, Poland; the Fundação para a Ciência e a Tecnologia, Portugal; JINR, Dubna; the Ministry of Education and Science of the Russian Federation, the Federal Agency of Atomic Energy of the Russian Federation, Russian Academy of Sciences, the Russian Foundation for Basic Research, and the National Research Center “Kurchatov Institute”; the Ministry of Education, Science and Technological Development of Serbia; the Secretaría de Estado de Investigación, Desarrollo e Innovación, Programa Consolider-Ingenio 2010, Plan Estatal de Investigación Científica y Técnica y de Innovación 2013–2016, Plan de Ciencia, Tecnología e Innovación 2013–2017 del Principado de Asturias, and Fondo Europeo de Desarrollo Regional, Spain; the Ministry of Science, Technology and Research, Sri Lanka; the Swiss Funding Agencies (ETH Board, ETH Zurich, PSI, SNF, UniZH, Canton Zurich, and SER); the Ministry of Science and Technology, Taipei; the Thailand Center of Excellence in Physics, the Institute for the Promotion of Teaching Science and Technology of Thailand, Special Task Force for Activating Research and the National Science and Technology Development Agency of Thailand; the Scientific and Technical Research Council of Turkey, and Turkish Atomic Energy Authority; the National Academy of Sciences of Ukraine, and State Fund for Fundamental Researches, Ukraine; the Science and Technology Facilities Council, UK; the US Department of Energy, and the US National Science Foundation.

Individuals have received support from the Marie-Curie programme and the European Research Council and Horizon 2020 Grant, contract Nos. 675440 and 765710 (European Union); the Leventis Foundation; the A.P. Sloan Foundation; the Alexander von Humboldt Foundation; the Belgian Federal Science Policy Office; the Fonds pour la Formation à la Recherche dans l’Industrie et dans l’Agriculture (FRIA-Belgium); the Agentschap voor Innovatie door Wetenschap en Technologie (IWT-Belgium); the F.R.S.-FNRS and FWO (Belgium) under the “Excellence of Science – EOS” – be.h project n. 30820817; the Beijing Municipal Science & Technology Commission, No. Z181100004218003; the Ministry of Education, Youth and Sports (MEYS) of the Czech Republic; the Lendület (“Momentum”) Programme and the János Bolyai Research Scholarship of the Hungarian Academy of Sciences, the New National Excellence Program ÚNKP, the NKfIA research grants 123842, 123959, 124845, 124850, and 125105 (Hungary); the Council of Scientific and Industrial Research, India; the HOMING PLUS programme of the Foundation for Polish Science, cofinanced from European Union, Regional Development Fund, the Mobility Plus programme of the Ministry of Science and Higher Education, the National Science Center (Poland), contracts Harmonia 2014/14/M/ST2/00428, Opus 2014/13/B/ST2/02543, 2014/15/B/ST2/03998, and 2015/19/B/ST2/02861, Sonata-bis 2012/07/E/ST2/01406; the National Priorities Research Program by Qatar National Research Fund; the Programa de Excelencia María de Maeztu, and the Programa Severo Ochoa del Principado de Asturias; the Thalís and Aristeia programmes cofinanced by EU-ESF, and the Greek NSRF; the Rachadapisek Sompot Fund for Postdoctoral Fellowship, Chulalongkorn University, and the Chulalongkorn Academic into Its 2nd Century Project Advancement Project (Thailand); the Welch Foundation, contract C-1845; and the Weston Havens Foundation (USA).



## References

- [1] ATLAS Collaboration, “Measurements of top-quark pair differential cross-sections in the lepton+jets channel in  $pp$  collisions at  $\sqrt{s} = 13$  TeV using the ATLAS detector”, *JHEP* **11** (2017) 191, doi:10.1007/JHEP11(2017)191, arXiv:1708.00727.
- [2] ATLAS Collaboration, “Measurements of top-quark pair differential cross-sections in the  $e\mu$  channel in  $pp$  collisions at  $\sqrt{s} = 13$  TeV using the ATLAS detector”, *Eur. Phys. J.* **C77** (2017), no. 5, 292, doi:10.1140/epjc/s10052-017-4821-x, arXiv:1612.05220.
- [3] ATLAS Collaboration, “Measurement of lepton differential distributions and the top quark mass in  $t\bar{t}$  production in  $pp$  collisions at  $\sqrt{s} = 8$  TeV with the ATLAS detector”, *Eur. Phys. J.* **C77** (2017), no. 11, 804, doi:10.1140/epjc/s10052-017-5349-9, arXiv:1709.09407.
- [4] ATLAS Collaboration, “Measurement of top quark pair differential cross-sections in the dilepton channel in  $pp$  collisions at  $\sqrt{s} = 7$  and 8 TeV with ATLAS”, *Phys. Rev.* **D94** (2016), no. 9, 092003, doi:10.1103/PhysRevD.94.092003, arXiv:1607.07281.
- [5] ATLAS Collaboration, “Differential top-antitop cross-section measurements as a function of observables constructed from final-state particles using  $pp$  collisions at  $\sqrt{s} = 7$  TeV in the ATLAS detector”, *JHEP* **06** (2015) 100, doi:10.1007/JHEP06(2015)100, arXiv:1502.05923.
- [6] ATLAS Collaboration, “Measurements of top quark pair relative differential cross-sections with ATLAS in  $pp$  collisions at  $\sqrt{s} = 7$  TeV”, *Eur. Phys. J.* **C73** (2013), no. 1, 2261, doi:10.1140/epjc/s10052-012-2261-1, arXiv:1207.5644.
- [7] CMS Collaboration, “Measurement of normalized differential  $t\bar{t}$  cross sections in the dilepton channel from  $pp$  collisions at  $\sqrt{s} = 13$  TeV”, *JHEP* **04** (2018) 060, doi:10.1007/JHEP04(2018)060, arXiv:1708.07638.
- [8] CMS Collaboration, “Measurements of normalised multi-differential cross sections for top quark pair production in  $pp$  collisions at  $\sqrt{s} = 13$  TeV and simultaneous determination of the strong coupling strength, top quark pole mass and parton distribution functions”, Technical Report CMS-PAS-TOP-18-004, CERN, Geneva, 2018.
- [9] CMS Collaboration, “Measurements of  $t\bar{t}$  differential cross sections in proton-proton collisions at  $\sqrt{s} = 13$  TeV using events containing two leptons”, *Submitted to: JHEP* (2018) arXiv:1811.06625.
- [10] CMS Collaboration, “Measurement of differential cross sections for top quark pair production using the lepton+jets final state in proton-proton collisions at 13 TeV”, *Phys. Rev.* **D95** (2017), no. 9, 092001, doi:10.1103/PhysRevD.95.092001, arXiv:1610.04191.
- [11] CMS Collaboration, “Measurements of differential cross sections of top quark pair production as a function of kinematic event variables in proton-proton collisions at  $\sqrt{s} = 13$  TeV”, *JHEP* **06** (2018) 002, doi:10.1007/JHEP06(2018)002, arXiv:1803.03991.
- [12] CMS Collaboration, “Measurement of double-differential cross sections for top quark pair production in  $pp$  collisions at  $\sqrt{s} = 8$  TeV and impact on parton distribution



- functions", *Eur. Phys. J.* **C77** (2017), no. 7, 459,  
doi:10.1140/epjc/s10052-017-4984-5, arXiv:1703.01630.
- [13] CMS Collaboration, "Measurement of the differential cross section for top quark pair production in pp collisions at  $\sqrt{s} = 8$  TeV", *Eur. Phys. J.* **C75** (2015), no. 11, 542,  
doi:10.1140/epjc/s10052-015-3709-x, arXiv:1505.04480.
- [14] CMS Collaboration, "Measurement of the differential cross sections for top quark pair production as a function of kinematic event variables in pp collisions at  $\sqrt{s}=7$  and 8 TeV", *Phys. Rev.* **D94** (2016), no. 5, 052006, doi:10.1103/PhysRevD.94.052006, arXiv:1607.00837.
- [15] CMS Collaboration, "Measurement of differential top-quark pair production cross sections in pp collisions at  $\sqrt{s} = 7$  TeV", *Eur. Phys. J.* **C73** (2013), no. 3, 2339,  
doi:10.1140/epjc/s10052-013-2339-4, arXiv:1211.2220.
- [16] ATLAS Collaboration, "Measurements of  $t\bar{t}$  differential cross-sections of highly boosted top quarks decaying to all-hadronic final states in pp collisions at  $\sqrt{s} = 13$  TeV using the ATLAS detector", *Phys. Rev.* **D98** (2018), no. 1, 012003,  
doi:10.1103/PhysRevD.98.012003, arXiv:1801.02052.
- [17] ATLAS Collaboration, "Measurement of the differential cross-section of highly boosted top quarks as a function of their transverse momentum in  $\sqrt{s} = 8$  TeV proton-proton collisions using the ATLAS detector", *Phys. Rev.* **D93** (2016), no. 3, 032009,  
doi:10.1103/PhysRevD.93.032009, arXiv:1510.03818.
- [18] CMS Collaboration Collaboration, "Measurement of the  $t\bar{t}$  production cross section at 13 TeV in the all-jets final state", Technical Report CMS-PAS-TOP-16-013, CERN, Geneva, 2016.
- [19] CMS Collaboration, "Measurement of the integrated and differential  $t\bar{t}$  production cross sections for high- $p_t$  top quarks in pp collisions at  $\sqrt{s} = 8$  TeV", *Phys. Rev.* **D94** (2016), no. 7, 072002, doi:10.1103/PhysRevD.94.072002, arXiv:1605.00116.
- [20] CMS Collaboration Collaboration, "Measurement of the differential  $t\bar{t}$  cross section with high- $p_T$  top-quark jets in the all-hadronic channel at  $\sqrt{s} = 8$  TeV", Technical Report CMS-PAS-TOP-16-018, CERN, Geneva, 2017.
- [21] CMS Collaboration, "The CMS experiment at the CERN LHC", *JINST* **3** (2008) S08004,  
doi:10.1088/1748-0221/3/08/S08004.
- [22] CMS Collaboration, "The CMS trigger system", *JINST* **12** (2017) P01020,  
doi:10.1088/1748-0221/12/01/P01020, arXiv:1609.02366.
- [23] P. Nason, "A new method for combining NLO QCD with shower Monte Carlo algorithms", *JHEP* **11** (2004) 040, doi:10.1088/1126-6708/2004/11/040, arXiv:hep-ph/0409146.
- [24] S. Frixione, P. Nason, and G. Ridolfi, "A Positive-weight next-to-leading-order Monte Carlo for heavy flavour hadroproduction", *JHEP* **09** (2007) 126,  
doi:10.1088/1126-6708/2007/09/126, arXiv:0707.3088.
- [25] S. Frixione, P. Nason, and C. Oleari, "Matching NLO QCD computations with parton shower simulations: the POWHEG method", *JHEP* **11** (2007) 070,  
doi:10.1088/1126-6708/2007/11/070, arXiv:0709.2092.

- [26] S. Alioli, P. Nason, C. Oleari, and E. Re, “A general framework for implementing NLO calculations in shower Monte Carlo programs: the POWHEG BOX”, *JHEP* **06** (2010) 043, doi:10.1007/JHEP06(2010)043, arXiv:1002.2581.
- [27] S. Alioli, S. O. Moch, and P. Uwer, “Hadronic top-quark pair-production with one jet and parton showering”, *JHEP* **01** (2012) 137, doi:10.1007/JHEP01(2012)137, arXiv:1110.5251.
- [28] S. Alioli, P. Nason, C. Oleari, and E. Re, “NLO single-top production matched with shower in POWHEG:  $s$ - and  $t$ -channel contributions”, *JHEP* **09** (2009) 111, doi:10.1088/1126-6708/2009/09/111, arXiv:0907.4076. [Erratum: doi:10.1007/JHEP02(2010)011].
- [29] J. Alwall et al., “The automated computation of tree-level and next-to-leading order differential cross sections, and their matching to parton shower simulations”, *JHEP* **07** (2014) 079, doi:10.1007/JHEP07(2014)079, arXiv:1405.0301.
- [30] J. Alwall et al., “Comparative study of various algorithms for the merging of parton showers and matrix elements in hadronic collisions”, *Eur. Phys. J. C* **53** (2008) 473–500, doi:10.1140/epjc/s10052-007-0490-5, arXiv:0706.2569.
- [31] T. Sjöstrand, S. Mrenna, and P. Z. Skands, “PYTHIA 6.4 physics and manual”, *JHEP* **05** (2006) 026, doi:10.1088/1126-6708/2006/05/026, arXiv:hep-ph/0603175.
- [32] T. Sjöstrand, S. Mrenna, and P. Z. Skands, “A brief introduction to PYTHIA 8.1”, *Comput. Phys. Commun.* **178** (2008) 852, doi:10.1016/j.cpc.2008.01.036, arXiv:0710.3820.
- [33] NNPDF Collaboration, “Parton distributions for the LHC Run II”, *JHEP* **04** (2015) 040, doi:10.1007/JHEP04(2015)040, arXiv:1410.8849.
- [34] CMS Collaboration, “Event generator tunes obtained from underlying event and multiparton scattering measurements”, *Eur. Phys. J. C* **76** (2015) 155, doi:10.1140/epjc/s10052-016-3988-x, arXiv:1512.00815.
- [35] CMS Collaboration, “Investigations of the impact of the parton shower tuning in Pythia 8 in the modelling of  $t\bar{t}$  at  $\sqrt{s} = 8$  and 13 TeV”, Technical Report CMS-PAS-TOP-16-021, CERN, Geneva, 2016.
- [36] GEANT4 Collaboration, “GEANT4—a simulation toolkit”, *Nucl. Instrum. Meth. A* **506** (2003) 250, doi:10.1016/S0168-9002(03)01368-8.
- [37] M. Czakon and A. Mitov, “Top++: A program for the calculation of the top-pair cross-section at hadron colliders”, *Comput. Phys. Commun.* **185** (2014) 2930, doi:10.1016/j.cpc.2014.06.021, arXiv:1112.5675.
- [38] Y. Li and F. Petriello, “Combining QCD and electroweak corrections to dilepton production in the framework of the FEWZ simulation code”, *Phys. Rev. D* **86** (2012) 094034, doi:10.1103/PhysRevD.86.094034, arXiv:1208.5967.
- [39] N. Kidonakis, “Top Quark Production”, (2014). arXiv:1311.0283.
- [40] M. Bahr et al., “Herwig++ Physics and Manual”, *Eur. Phys. J. C* **58** (2008) 639–707, doi:10.1140/epjc/s10052-008-0798-9, arXiv:0803.0883.

- [41] S. Gieseke, C. Rohr, and A. Siodmok, “Colour reconnections in Herwig++”, *Eur. Phys. J. C* **72** (2012) 2225, doi:10.1140/epjc/s10052-012-2225-5, arXiv:1206.0041.
- [42] CMS Collaboration, “Particle-flow reconstruction and global event description with the cms detector”, *JINST* **12** (2017) P10003, doi:10.1088/1748-0221/12/10/P10003, arXiv:1706.04965.
- [43] M. Cacciari, G. P. Salam, and G. Soyez, “The anti- $k_t$  jet clustering algorithm”, *JHEP* **04** (2008) 063, doi:10.1088/1126-6708/2008/04/063, arXiv:0802.1189.
- [44] M. Cacciari, G. P. Salam, and G. Soyez, “FastJet user manual”, *Eur. Phys. J. C* **72** (2012) 1896, doi:10.1140/epjc/s10052-012-1896-2, arXiv:1111.6097.
- [45] CMS Collaboration, “Jet energy scale and resolution in the CMS experiment in pp collisions at 8 TeV”, *JINST* **12** (2017) P02014, doi:10.1088/1748-0221/12/02/P02014, arXiv:1607.03663.
- [46] J. Thaler and K. Van Tilburg, “Identifying boosted objects with  $N$ -subjettiness”, *JHEP* **03** (2011) 015, doi:10.1007/JHEP03(2011)015, arXiv:1011.2268.
- [47] Y. L. Dokshitzer, G. D. Leder, S. Moretti, and B. R. Webber, “Better jet clustering algorithms”, *JHEP* **08** (1997) 001, doi:10.1088/1126-6708/1997/08/001, arXiv:hep-ph/9707323.
- [48] M. Wobisch and T. Wengler, “Hadronization corrections to jet cross-sections in deep inelastic scattering”, in *Proceedings of the Workshop on Monte Carlo Generators for HERA Physics, Hamburg, Germany*, p. 270. 1998. arXiv:hep-ph/9907280.
- [49] M. Dasgupta, A. Fregoso, S. Marzani, and G. P. Salam, “Towards an understanding of jet substructure”, *JHEP* **09** (2013) 029, doi:10.1007/JHEP09(2013)029, arXiv:1307.0007.
- [50] J. M. Butterworth, A. R. Davison, M. Rubin, and G. P. Salam, “Jet substructure as a new Higgs search channel at the LHC”, *Phys. Rev. Lett.* **100** (2008) 242001, doi:10.1103/PhysRevLett.100.242001, arXiv:0802.2470.
- [51] A. J. Larkoski, S. Marzani, G. Soyez, and J. Thaler, “Soft drop”, *JHEP* **05** (2014) 146, doi:10.1007/JHEP05(2014)146, arXiv:1402.2657.
- [52] CMS Collaboration, “Identification of heavy-flavour jets with the CMS detector in pp collisions at 13 TeV”, *JINST* **13** (2018) P05011, doi:10.1088/1748-0221/13/05/P05011, arXiv:1712.07158.
- [53] J. Therhaag, “TMVA Toolkit for multivariate data analysis in ROOT”, *PoS ICHEP2010* (2010) 510, doi:10.22323/1.120.0510.
- [54] W. Verkerke and D. P. Kirkby, “The RooFit toolkit for data modeling”, *eConf C0303241* (2003) MOLT007, arXiv:physics/0306116. [186(2003)].
- [55] CMS Collaboration Collaboration, “CMS Luminosity Measurements for the 2016 Data Taking Period”, Technical Report CMS-PAS-LUM-17-001, CERN, Geneva, 2017.
- [56] S. Schmitt, “TUnfold: an algorithm for correcting migration effects in high energy physics”, *JINST* **7** (2012) T10003, doi:10.1088/1748-0221/7/10/T10003, arXiv:1205.6201.